XLF/Cernunnos loss impairs mouse brain development by altering symmetric proliferative divisions of neural progenitors

Amandine Bery, Olivier Etienne, Laura Mouton, Sofiane Mokrani, Christine Granotier-Beckers, Laurent Gauthier, Justyne Feat-Vetel, Thierry Kortulewski, Elodie Pérès, Chantal Desmaze, et al.

Cell Reports

CellPress
OPEN ACCESS

Article

XLF/Cernunnos loss impairs mouse brain development by altering symmetric proliferative divisions of neural progenitors

Amandine Bery,[1,2,8,9] Olivier Etienne,[1,2,9] Laura Mouton,[1,2] Sofiane Mokrani,[1,2] Christine Granotier-Beckers,[1,2] Laurent R. Gauthier,[1,2] Justyne Feat-Vetel,[1,2] Thierry Kortulewski,[1,2] Elodie A. Pérès,[1,2,3] Chantal Desmaze,[1,2] Philippe Lestaveal,[4] Vilma Barroca,[1,2] Antony Laugeray,[5] Fawzi Boumezbeur,[3] Vincent Abramovski,[7] Stéphane Mortaud,[5,6] Arnaud Menuet,[5,6] Denis Le Bihan,[3] Jean-Pierre de Villartay,[7] and François D. Boussin[1,2,10,*]

[1]Université Paris Cité, Inserm, CEA, Stabilité Génétique Cellules Souches et Radiations/iRCM, 92265 Fontenay-aux-Roses, France
[2]Université Paris-Saclay, Inserm, CEA, Stabilité Génétique Cellules Souches et Radiations/iRCM, 92265 Fontenay-aux-Roses, France
[3]NeuroSpin, CEA, CNRS, Université Paris-Saclay, Gif-sur-Yvette, France
[4]Institut de Radioprotection et de Sûreté Nucléaire (IRSN), PSE-SANTE/SERAMED, 92262 Fontenay-aux-Roses, France
[5]Immunologie et Neurogénétique Expérimentales et Moléculaires – UMR7355 CNRS – 3B, rue de la Férollerie, 45071 Orléans, France
[6]Université d'Orléans, Orléans, France
[7]Université Paris Cité, *Imagine* Institute, Laboratory "Genome Dynamics in the Immune System", Equipe labellisée La LIGUE, INSERM UMR 1163, 75015 Paris, France
[8]Present address: Université de Strasbourg, INCI UPR3212, Strasbourg, France
[9]These authors contributed equally
[10]Lead contact
*Correspondence: francois.boussin@cea.fr
https://doi.org/10.1016/j.celrep.2023.112342

SUMMARY

XLF/Cernunnos is a component of the ligation complex used in classical non-homologous end-joining (cNHEJ), a major DNA double-strand break (DSB) repair pathway. We report neurodevelopmental delays and significant behavioral alterations associated with microcephaly in *Xlf*−/− mice. This phenotype, reminiscent of clinical and neuropathologic features in humans deficient in cNHEJ, is associated with a low level of apoptosis of neural cells and premature neurogenesis, which consists of an early shift of neural progenitors from proliferative to neurogenic divisions during brain development. We show that premature neurogenesis is related to an increase in chromatid breaks affecting mitotic spindle orientation, highlighting a direct link between asymmetric chromosome segregation and asymmetric neurogenic divisions. This study reveals thus that XLF is required for maintaining symmetric proliferative divisions of neural progenitors during brain development and shows that premature neurogenesis may play a major role in neurodevelopmental pathologies caused by NHEJ deficiency and/or genotoxic stress.

INTRODUCTION

Numerous human neurologic syndromes result from defective DNA damage signaling and compromised genome integrity.[1] DNA double-strand breaks (DSBs) may arise spontaneously in the developing brain from various endogenous sources, including replicative or oxidative stress and transcriptional activity.[2–4] Recurrent DSB clusters have been identified in dividing neural progenitors, which may underlie the diversity of neuronal cell types.[5,6] Embryonic mouse neural stem and progenitor cells (NSPCs) can face DSBs more efficiently than other embryonic cells and show a better resistance to chronic genotoxic stress.[7] These data suggest that their DNA damage response allows them both to preserve their genome stability and to generate neuronal genetic diversity.

Classical non-homologous end-joining (cNHEJ), the main DSB repair pathway in mammalian cells, performs the direct religation of broken DNA ends. cNHEJ involves the Ku70/80 heterodimer (Ku) that binds to DNA ends and recruits the DNA-dependent protein kinase catalytic subunit (DNA-PKcs) generating the DNA-PK holoenzyme. DNA-PK promotes synapsis of DNA ends, enhances appropriate end processing through activation of the Artemis endo/exo-nuclease, and recruits the ligation complex made of X-ray cross-complementing protein 4 (XRCC4), DNA ligase IV (LigIV), and XRCC4-like factor (XLF, also known as Cernunnos or NHEJ1).[8,9] cNHEJ is an integral part of the V(D)J recombination machinery, which generates a diverse antigenic repertoire during T and B cell development. Mutations in Artemis, DNA-PKcs, LigIV, and XLF cause various extents of severe combined immunodeficiency (SCID) in humans partly due to impaired V(D)J recombination.[9–12]

Patients with LigIV, XRCC4 or XLF deficiencies developed microcephaly, associated with neurodevelopmental impairments including low to profound learning deficit.[11,13,14]

Confirming the importance of cNHEJ for brain development, the loss of LigIV and XRCC4 is lethal *in utero* in mice because of an abnormal neuronal cell death.[8,9,15–18] By contrast, *Xlf*−/− mice are viable. Only a scarce neuronal cell death occurred at embryonic stages[19] and adults show a slightly affected immune system.[20–23] Consistently with a DNA repair defect, *Xlf*−/− murine neural progenitors are more sensitive to genotoxic stress as compared with wild-type (WT) cells. They also show spontaneous cytogenetic abnormalities, but at levels that do not alter their growth *in vitro* suggesting that the DNA repair defect is low.[7]

The mild phenotype of *Xlf*−/− mice has thus been shown to rely on compensating pathways from the ATM-dependent DNA damage response[24] and on overlapping functions between the V(D)J recombinase protein RAG2 and XLF during V(D)J recombination, lymphocyte development, and the maintenance of genome stability.[25] Furthermore, XLF shares one or more redundant functions with PAXX, another cNHEJ repair factor, as, unlike *Paxx*−/− or *Xlf*−/− single mutants, mice lacking both proteins died *in utero* with an extensive cell death in the central nervous system, similar to *Xrcc4*−/− or *LigIV*−/− embryos.[26,27]

Here, we show that the loss of XLF severely impairs the mouse brain development and functions leading to a phenotype reminiscent of clinical and neuropathologic findings in humans deficient in cNHEJ. We further demonstrate that this results primarily from a premature neurogenesis caused by an increased chromosome instability in neural progenitors that reduces their proliferative, symmetric divisions, limiting further brain development.

RESULTS

Microcephalia and microstructural alterations in *Xlf*−/− adult mice

Adult *Xlf*−/− mice have a body weight in the range of WT controls, but are smaller[21] and have a significantly lower brain weight (Figure 1A). Anatomic T_2*-weighted magnetic resonance imaging (MRI) showed that the whole brain volume of adult *Xlf*−/− mice was significantly decreased by nearly 8% as compared with WT controls. In addition, the volumes of gray (GM) and white matters (WM) were decreased by nearly 9% and 5%, respectively, without any significant variation of the cerebrospinal fluid (CSF) volume (Figure 1B). *Xlf* deficiency affected all the segmented regions of interest (ROIs) with larger decreases in the cortex (−9%) and the corpus callosum (−8%) (Figure 1C). Altogether, MRI analyzes evidence a mild microcephaly in *Xlf*−/− mice.

In order to determine whether microcephaly was associated with microstructural alterations, we investigated the extent and complexity of cortical myelination patterns in 3-month-old mice using previously described methods.[28] We showed a significant reduction in myelin basic protein (MBP) area in the cortex of *Xlf*−/− mice as compared with WT animals (Figures 1D and 1E). The increase in coherency of cortical myelinated axons, which is as an inverse measure of arborization/complexity of myelinated patterns, revealed a reduced complexity of the cortical myelination pattern in *Xlf*−/− mice, which was further confirmed by fiber tracing showing reductions in fiber length and in the number of intersections (Figures 1F–1H).

Neurodevelopmental delays and behavioral impairments in *Xlf*−/− mice

In order to determine the consequences of *Xlf* deficiency for brain development and functions, we first investigated the postnatal developmental patterns of newborn mice. Neurodevelopmental reflexes were thus assessed during the pre-weaning period using different sensorimotor tests to appreciate brain maturation. The acquisition of the surface righting reflex was delayed by 3 days in these mice as compared with WT controls (Figure 2A). Furthermore, they failed the negative geotaxis and the cliff avoidance tests at PN9, when WT pups had already acquired these reflexes at PN6 (Figures 2B and 2C). Consequently, these three tests revealed significant neurodevelopmental delays in *Xlf*−/− pups.

We then compared the behavior of adult (3-month-old) *Xlf*−/− mice with that of WT controls by using several assays assessing their locomotor activity, stress state, memory, and sociability.

The open-field exploration test[29] revealed a significant reduction of ambulatory exploration in adult *Xlf*−/− mice, as indicated by the decrease of total distance they traveled and the increase in immobility during the 5-min trial (Figure 2D). In the rotarod test, which consisted of placing mice on a rotating rod with a steady acceleration, a reduced speed at fall revealed a decreased sensorimotor coordination in *Xlf*−/− mice[30] (Figure 2E).

Xlf−/− mice did not display any difference in the time spent in the anxiogenic center part of the open-field (Figure 2D). Consistently, they spent similar times as WT mice in the anxiogenic open arm of the elevated plus maze, showing no particular increase in anxiety (Figure 2F); however, their immobility in the forced swim test (FST) throughout the trial period suggests a despair-like or depression-like behavior (Figure 2G).[31]

The novel object recognition task was used to evaluate cognition. Mice were presented with two similar objects, and then one of the familiar objects was replaced by a new object during the next session. As shown in Figure 2H, *Xlf*−/− mice failed to discriminate between the familiar and the new object, revealing an impaired recognition memory.[32] They also showed a reduced spontaneous alternation behavior in the Y-maze, an index of short-term memory, suggesting a reduced working memory (Figure 2I).[33]

Finally, the three-chamber sociability test[34] was used to document voluntary initiation of social interactions. During the first 5-min trial of this test, mice were let free to explore the entire three-chamber apparatus. As previously observed with the open-field test, the *Xlf*−/− mice traveled a shorter total distance than WT mice (data not shown), confirming their decreased exploratory activity. In the second trial, an unfamiliar mouse was put under a wire cup in one side chamber and an inert object placed under an identical wire cup was placed in the other side chamber. The central chamber remained empty. Mice were left free to explore and initiate social contacts for 5 min. WT mice spent significantly more time in the chamber containing the mouse than in the chamber containing the object or the center chamber (Figure 2F), revealing their preference for social interactions in accordance with previous data.[35] By contrast, *Xlf*−/− mice did not significantly display this preference for the mouse-containing chamber, attesting a clear deficiency for social interactions (Figure 2J). In the third 5-min trial, the object

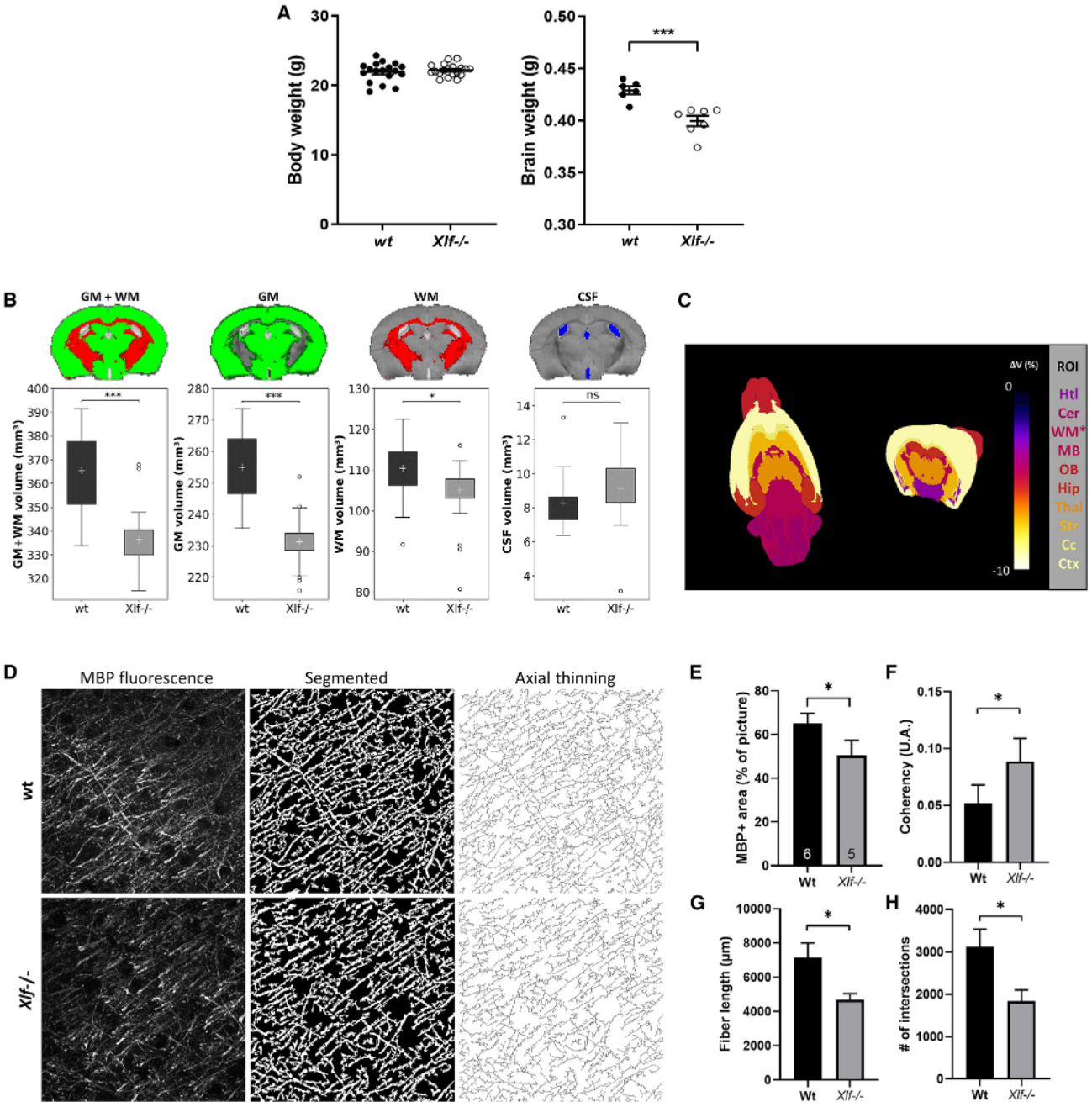

Figure 1. Mild microcephaly and microstructural alterations in *Xlf*−/− adult mice

(A) Left, body weight of WT (n = 18) and *Xlf*−/− (n = 19) 4-month-old mice. Right, brain weight of WT (n = 6) and *Xlf*−/− (n = 7) 4-month-old mice. Mean weight ± SEM, ***p < 0.001, Mann-Whitney test.

(B) MRI analyses performed on WT (n = 21) and *Xlf*−/− (n = 31) 3-month-old male mice. Top: Brain, gray matter (GM), white matter (WM), and cerebrospinal fluid (CSF) masks overlaid on the mouse brain template Turone Mouse Brain Template Atlas (TMBTA) visualized on a coronal slice. Bottom: Brain, GM, WM, and CSF absolute volumes in WT and *Xlf*−/− mice. The cross represents the mean. The box extends from the first to the third quartile and the whiskers delimit the confidence range.

(C) Three-dimensional representation of the local brain atrophies at the regions of interest (ROI) scale. The color bar codes for the volume variation amplitude $\Delta V = (V_{Xlf-/-} - V_{wt})/V_w$, with V being the mean volume of the considered ROI.

(D) Reduced complexity of the cortical myelination pattern in *Xlf*−/− mice. On the left, the original images of MBP signal, in the middle the segmented images extracted from the original images, and on the right the axial thinning maps as calculated from the segmented images.

(E) Bar graphs showing a decrease in MBP+ area in *Xlf*−/− mice.

(F) Increased coherency of myelinated axons in *Xlf*−/− mice.

(G and H) Bar graphs showing decreased length (G) and reduced number of intersections (H) of myelinated axons in *Xlf*−/− mice.

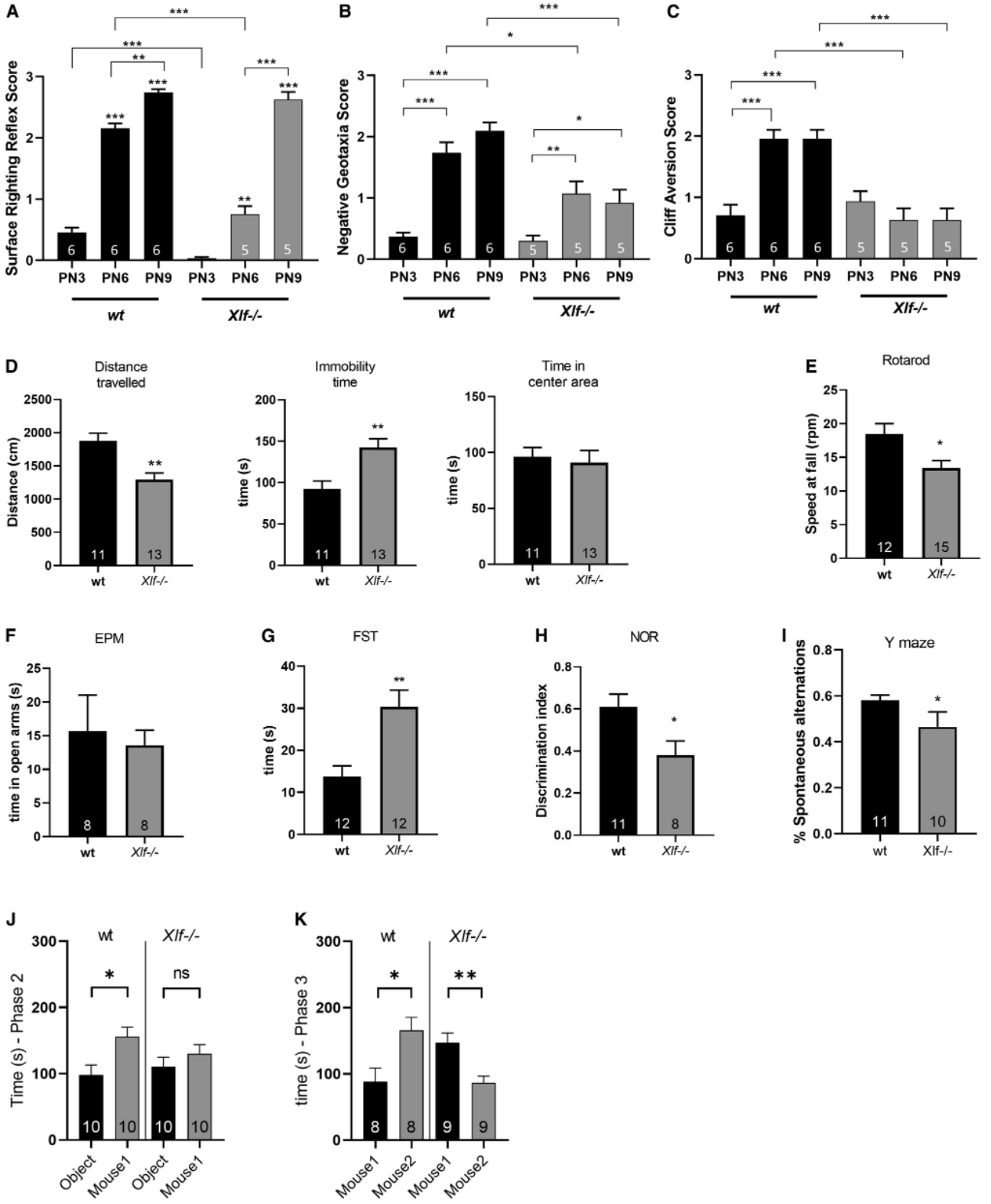

(legend on next page)

was replaced by a new mouse (mouse 2). Contrary to WT mice, *Xlf*−/− mice did not spend longer times with mouse 2, clearly showing their lack of preference for social novelty (Figure 2K).

These data clearly demonstrate that microcephaly and microstructural alterations are associated with neurodevelopmental delay and significant cognitive and behavioral impairments in *Xlf*−/− mice.

Slow growth rate of the cerebral cortex in *Xlf*−/− embryos

We next investigated the fetal brain development of *Xlf*−/− mice, especially corticogenesis. Consistently with the microcephaly found in adults, results showed that the cerebral cortex thickness of *Xlf*−/− embryos increased at a slower rate than that of WT embryos (Figures 3A–3C).

Neural progenitor proliferation, migration, and differentiation are strictly regulated spatially and temporally during brain development. During early corticogenesis, the radial glial cells (RGC) expand in the ventricular zone (VZ) by symmetric divisions.[36] Then, they predominantly perform asymmetric neurogenic divisions: they generate an RGC to maintain the proliferative pool, and either a neuron that migrate through the intermediate zone (IZ) to reach the cortical plate (CP) or an intermediate progenitor cell (IPC). The IPCs migrate to an overlying proliferating layer, the subventricular zone (SVZ), and ultimately generate a pair of neurons.[37] Interestingly, immunostaining of Pax6 a marker of neural progenitors,[38] revealed that the cortical proliferative zones (VZ + SVZ) of *Xlf*−/− embryos was systematically smaller than that of WT controls at different developmental stages (Figures 3B and 3D). This was associated with a lower thickness of the CP (Figures 3B and 3E).

Immunostaining of the cortical layer markers CUX1 (layers 2–4) and CTIP2 (layers 5–6) in postnatal and adult brains (Figures 3E–3G) revealed that the numbers of neurons expressing these markers were significantly decreased, and therefore an altered cortical patterning in both the postnatal and adult *Xlf*−/− brains. By contrast, the number and density of oligodendrocytes were similar in *Xlf*−/− and WT mice suggesting that oligodendrogenesis may not be severely impacted by Xlf loss (Figure S1).

Altogether these data show that *Xlf* deficiency affects the neural progenitor compartment and neuron production, leading us to further investigate the effects of *Xlf* deletion on neurogenesis.

Low apoptosis in the brain of *Xlf*−/− embryos

Apoptosis in the developing brain is a well-known cause of microcephaly; we thus quantified the number of apoptotic cells in the embryonic *Xlf*−/− brains from the developmental stages E12.5 to E15.5 (Figure 4). In accordance with previous reports,[19,20,26] no massive apoptosis was detected in the embryonic *Xlf*−/− brains, differing in that from *LigIV*−/−, *Xrcc4*−/− or *Paxx*/*Xlf*−/− embryos.[15,19,39] As shown in Figures 4A and 4B, apoptosis remained at levels <40 times lower than apoptosis found in *Paxx*−/−*Xlf*−/− embryos (E15.5). Nevertheless, XLF loss was associated with a slight but significant increase of apoptosis as compared with WT embryos (Figures 4A–4C). Apoptotic cells were detected throughout the developing cortex of *Xlf*−/− brains, but mainly outside the VZ in the newly generated overlying layers (i.e., IZ and CP, Figure 4C), suggesting that apoptosis occurs primarily in newborn neurons as previously reported in other cNHEJ-deficient mouse settings.[15,40]

To ascertain the DNA repair defects in *Xlf*−/− neural cells, we exposed the *Xlf*−/− embryos *in utero* to low dose of ionizing radiation (10, 50, and 100 mGy) at E14.5 and quantified apoptosis in the developing brain 4 h later.[41] The increase of apoptosis in the embryonic *Xlf*−/− brains as compared with WT controls after *in utero* irradiation clearly show the DNA repair defect in *Xlf*−/− neural cells (Figure S2).

In order to investigate the possibility that the scarce neuronal apoptosis in the developing cortex causes the microcephaly in *Xlf*-deficient mice, we analyzed *p53*−/−*Xlf*−/− embryos. Consistently with previous reports showing that p53 mediates neuronal apoptosis related to an NHEJ defect,[42,43] the basal level of apoptotic cells in the double knockout (KO) embryonic brains was significantly lower than that of *p53*+/+*Xlf*−/− embryos and similar to that found in controls (WT and *p53*−/−*Xlf*+/+ embryos) (Figure 4D). Interestingly, the thicknesses of the total cortex, the proliferative zone (VZ + SVZ), and the CP were significantly decreased in *p53*−/−*Xlf*−/− embryos, as compared with WT embryos (Figure S3). Except for the CP, these decreases were in the same extent as that in *p53*+/+*Xlf*−/− embryos, showing that other causes than apoptosis are involved in the microcephaly of *Xlf*−/− mice.

Premature neurogenesis in the brain of *Xlf*−/− embryos

Consistently with the reduced size of the neural progenitor compartment and the slower cortical growth rate in *Xlf*−/−

Figure 2. Neurodevelopmental delays in *Xlf*−/− mice

(A–C) Disruption in early sensorimotor development of postnatal *Xlf*−/− mice. During the pre-weaning period, brain maturation of the developing pups was assessed with different sensorimotor tests: the surface righting reflex (A), the negative geotaxis reflex (B), and the cliff avoidance test (C). The bar graphs show the score ± SEM obtained by pups from five litters per strain minimum. *Xlf*−/− postnatal mice showed a delay in surface righting reflex acquisition and failed the negative geotaxis reflex and the cliff aversion test. The numbers of mice analyzed are given inside the histogram bars. ***p < 0.001, **p < 0.01, *p < 0.05, Mann-Whitney test.

(D–K) Behavioral assays performed on adult mice (3 to 4 months old). (D): Abnormal exploratory activity in the open-field test. Mean distance traveled ± SEM (left), the immobility time ± SEM (middle), and time spent in the center ± SEM (right) by *Xlf*−/− mice and WT controls during the 5-min trial in the open-field were used as an index of ambulatory exploration. (E) *Xlf*−/− mice performed worse compared with WT animals on the rotarod task, indicating impaired motor coordination. (F) On the elevated plus maze, no significant differences were found in WT and *Xlf*−/− mice. (G) Mean immobility time ± SEM spent by *Xlf*−/− mice and WT controls in the forced swim test (FST). (H) *Xlf*−/− mice failed to discriminate between the familiar and the new object, revealing an impaired recognition memory on the novel object recognition task. (I) Xlf−/− mice show a decrease in the spontaneous alternations percentage compared with the WT mice on the Y-maze, suggesting a reduced working memory. (J and K) Sociability of WT and *Xlf*−/− mice was challenged in the three-chamber sociability test. (J) Phase 2, the bar graph shows the times ± SEM the mice spent in the chambers containing the object, in the one containing the mouse during the sociability phase. WT mice spent more time in the chamber containing the mouse, contrary to *Xlf*−/− mice. (K) Phase 3, a new mouse replaced the object. WT mice spent more time with the new mouse contrary to *Xlf*−/− mice. ***p < 0.001, **p < 0.01, *p < 0.05, Mann-Whitney test.

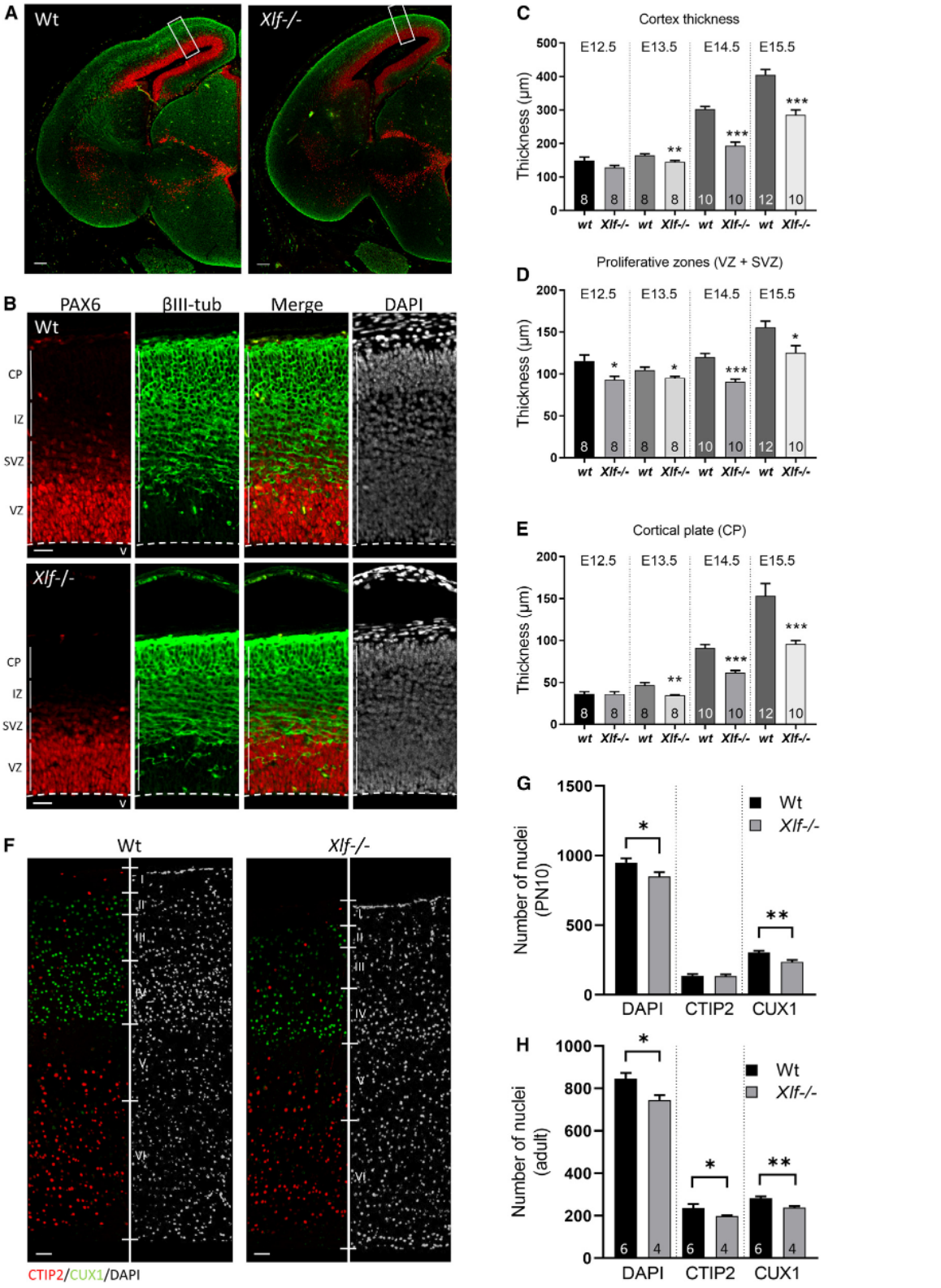

(legend on next page)

embryos shown above, we observed an increase of cell cycle exit of neural progenitors in *Xlf*−/− embryos (Figure 5A) as compared with WT controls. Similarly, quantification of phospho-H3-positive apical mitoses from E12.5 to E14.5 (Figure 5B) showed that the number of mitotic RGCs (apical mitoses) was reduced in *Xlf*−/− embryos, whereas that of basal mitoses in the SVZ was not significantly changed.

We thus investigated whether the XLF loss affects the mode of division of neural progenitors. Symmetrical vs. asymmetrical division of neural progenitors not only specifies the fate of daughter cells but also controls progenitor expansion and differentiation and eventually the cortical size.[45] The orientation of the cleavage plane of mitotic RGCs along the ventricular surface influences the degree of asymmetry in cell division: a vertical plane is associated with a symmetric division of RGCs while a horizontal plane signs an asymmetric neurogenic division.[46] Interestingly, we found that the mean of angles formed by the segregation line of daughter chromosomes and the ventricular surface[47,48] was significantly decreased in *Xlf*−/− embryos as compared with WT embryos at E12.5, E13.5, and E14.5 (Figures 5C and 5D). Importantly, similar results were obtained with *p53*−/−*Xlf*−/− embryos (Figure 5E). This suggests that *Xlf* loss induced an early switch of some RGCs from proliferative toward neurogenic divisions independently of the *p53* status, limiting therefore RGC expansion.

In order to further confirm the impact of *Xlf* deficiency on neurogenesis, we electroporated eGFP expression vector (pEBV-CAGeGFP-Bsd) *in utero* into cortical neural progenitors at E13.5. eGFP detection allowed us to investigate the fate of neural progenitors in the developing brain as previously described[49] (Figure 5F). Twenty-four hours after *in utero* electroporation, the *Xlf*−/− eGFP+ cells migrated farther from the ventricle and were significantly more abundant in the IZ than WT eGFP+ cells (Figure 5G), confirming the increased trend of *Xlf*−/− neural progenitors for neurogenic, rather than proliferative divisions.

Interestingly, DNA damage has been reported to induce the differentiation of neural progenitors.[50] Consistently, exposition of WT embryos electroporated with the eGFP expression vector to a sublethal dose of ionizing radiation (0.5 Gy, Figures 5F, 5G, and S2C) increased the migration of EGFP+ cells outside the proliferative zone, as observed in untreated *Xlf*−/− mice. These results emphasize the importance of unrepaired DNA damage in premature neurogenesis observed in *Xlf*−/− embryonic brains.

Finally, to determine whether the effects of *Xlf* deficiency on the mode of division of neural progenitors was cell autonomous, we investigated the consequences of the loss of *Xlf* specifically in RGCs during cortical development. To this end, we used Glast-CreERT2;*Xlf*$^{fl/fl}$;R26R-YFP mouse embryos, in which both *Xlf* deletion and YFP expression are initiated by tamoxifen-mediated activation of the Cre recombinase in RGC (i.e., Glast-expressing cells). YFP immunodetection allowed the tracking of *Xlf*−/− RGC and of their progeny (*Xlf*−/− YFP+ cells) in a WT context (Figure 5H). Glast-CreERT2;*Xlf*$^{WT/WT}$;R26R-YFP embryos in which tamoxifen treatment induces the permanent expression of YFP in Glast-positive *Xlf*$^{+/+}$ RGCs and in their progeny, were used as controls. Pregnant mice were treated with tamoxifen at E12.5 and YFP+ cell localization was analyzed in cortical slices at E14.5. Higher percentages of *Xlf*−/− YFP+ cells have lost Pax6 expression (Figure 5I) and were found in the IZ/CP (Figure 5J) as compared with WT YFP+ cells. Altogether, these data confirmed that XLF loss induced premature neurogenesis in a cell autonomous manner.

Asymmetric chromosome segregation in Xlf−/− neural progenitors

We have previously reported that *Xlf* deficiency led to a low chromosome instability in cultured *Xlf*−/− neural progenitors.[7] Quantification of 53BP1 foci in the medial part of the dorsal telencephalon at E14.5 showed a significant increase of DSBs in the VZ/SVZ and IZ of *Xlf*−/− embryos as compared with WT controls (Figures 6A–6C).

Therefore, to further investigate the implication of DNA repair deficiency in premature neurogenesis in *Xlf*−/− mice, we assessed the chromosome stability of neural progenitors *in vivo*. To this end, we performed a karyotyping analysis by Telo-FISH on metaphases collected without any culture step from the cortex of *Xlf*−/− and WT embryos at different developmental stages (Figure 6). This method has the advantage to directly reflect the *in vivo* situation without introducing the bias of DNA damage induced during cell cycle progression in culture conditions.

Metaphases of WT neural progenitors showed relatively high levels of chromosome aberrations at early cortical development stages with 0.18 ± 0.05 and 0.18 ± 0.04 aberrations per metaphase at E12.5 at E13.5, respectively. This frequency decreased then to 0.06 ± 0.03 at E14.5 and 0.04 ± 0.02 aberrations per metaphase at E15.5. Very few aberrations were chromosome-type, such as chromosome breaks, related to DSBs generated before DNA replication. Chromosome instability was indeed characterized by an elevated frequency of chromatid breaks, i.e., chromatid-type aberrations resulting from DSBs generated during or after replication, in late S or G2 phases (Figures 6D and 6E).

Chromosome instability was significantly increased in *Xlf*−/− neural progenitors, peaking at 0.36 ± 0.07 chromosome aberrations per metaphase at E13.5 as compared with 0.06 ± 0.03 in WT cells. Interestingly, as for WT neural progenitors, these aberrations were mostly chromatid breaks (Figure 6E), showing the importance of XLF during S or G2 phases for chromosome stability.

Figure 3. Slow growth rate of the cerebral cortex in *Xlf*−/− embryos

(A) Coronal sections of the cortex of E14.5 WT and *Xlf*−/− embryos stained with DAPI (gray) and antibodies directed against Pax6 (red) and ßIII-Tubulin (green). Scale bar, 100 μm.

(B) Higher magnification as delimited by white box. V, ventricle. Scale bar, 50 μm. Mean thickness of the dorsal telencephalon ± SEM.

(C–E) The VZ + SVZ, delineated by Pax6 expression (D), and the CP, delineated based on DAPI and ßIII-Tubulin (ßIII-tub) expression (E) of WT and *Xlf*−/− embryos determined on coronal slices at different developmental stages. n, number of embryos analyzed from at least three different litters.

(F–H) Coronal sections of the cortex of adult WT and *Xlf*−/− brains stained with DAPI (gray) and antibodies directed against CTIP2 (red) and CUX1 (green). Scale bar, 50 μm. Number of nuclei stained with DAPI, CTIP2, and CUX1 in PN10 brains (G) and adult brains (H). ***p < 0.001, **p < 0.01, *p < 0.05, Mann-Whitney test.

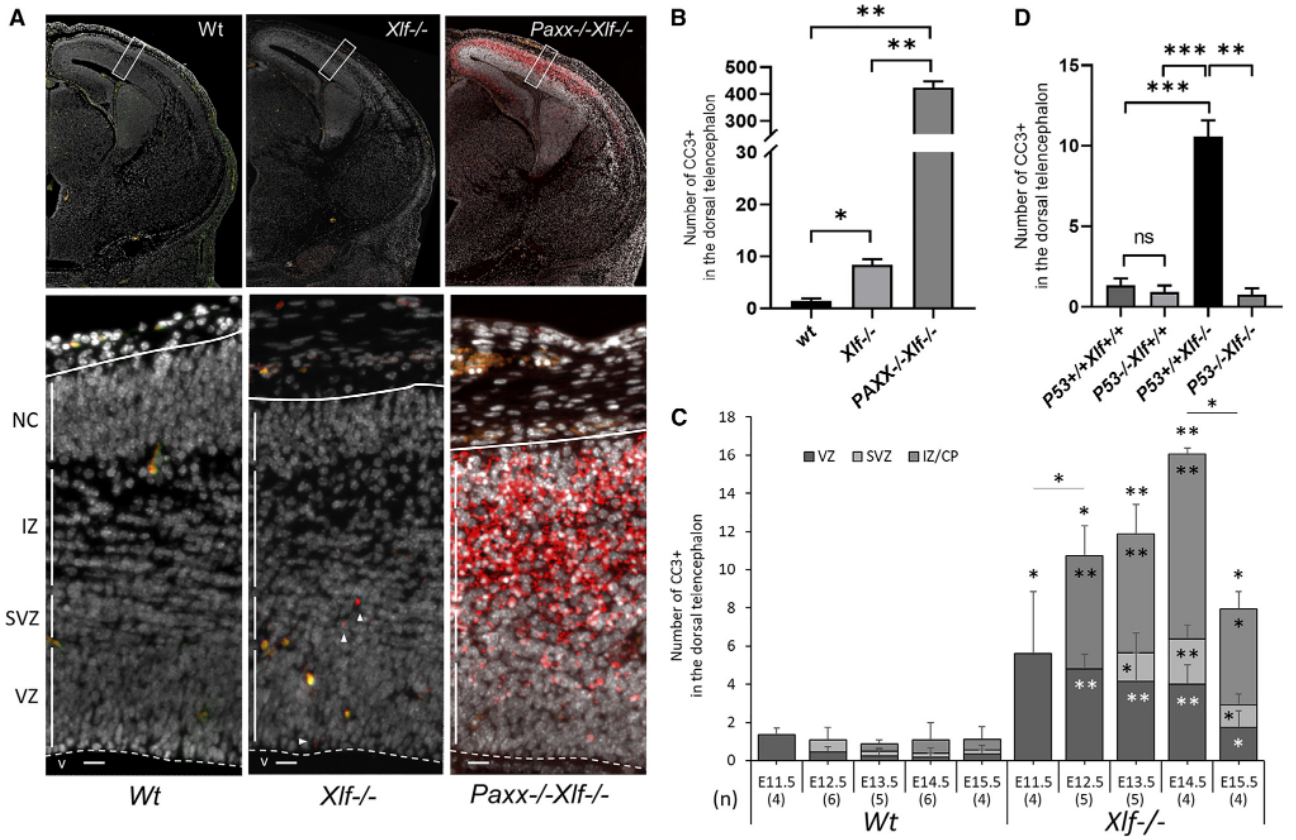

Figure 4. Low apoptosis and premature neurogenesis in the brain of *Xlf*−/− embryos

(A) Coronal sections of cerebral hemispheres of WT, *Xlf*−/−, *Paxx*−/−*Xlf*−/− embryos and collected at E15.5 and stained with DAPI (gray) and CC3 (red). Blood vessels are colored in orange. White box indicates the zone of higher magnification below. V, ventricle. Scale bar, 20 μm.

(B) Number of cleaved caspase 3-positive cells in the dorsal telencephalon of WT, *Xlf*−/−, and *Xlf*−/−*Paxx*−/− embryos.

(C) The bar graph shows the mean number of cleaved caspase 3-positive cells ± SEM detected per cortical slice in the different layers of the dorsal telencephalon of *Xlf*−/− and WT embryos from E11.5 to E15.5. (n), number of embryos obtained from at least two different litters. Stars inside the bars indicate the statistical significance between the mean number of apoptotic cells found in each cortical layer *Xlf*−/− and in the WT embryos. Stars just above the bars indicate the statistical (Mann-Whitney test) significance between the total number of apoptotic cells found in *Xlf*−/− dorsal telencephalon and that found in the WT controls.

(D) The bar graph shows the mean number of cleaved caspase 3-positive cells ± SEM detected per cortical slice in the different layers of the dorsal telencephalon of *p53*+/+*Xlf*−/−, *p53*−/−*Xlf*−/−, *p53*+/+*Xlf*+/+, and *p53*−/−*Xlf*+/+ embryos at E14.5. ***p < 0.001, **p < 0.01, *p < 0.05. Mann-Whitney test.

As shown in Figure 6F, most aberrant metaphases of WT and *Xlf*−/− neural progenitors contained only one chromatid break, which leads to an asymmetric chromosome segregation at anaphase: one daughter cell inheriting an intact chromosome and the other one a terminally deleted chromosome. Terminally deleted chromosomes result at the next metaphases in chromosome-type aberrations, such as chromosome breaks, i.e., chromosomes with terminal deletion on both chromatids, or dicentric chromosomes (resulting from the fusion of the terminally deleted chromosome with another one). Therefore, the low levels of chromosome-type aberrations in *Xlf*−/− neural progenitors clearly show that most daughter cells that inherited the terminally deleted chromosome stopped to divide, then differentiated and/or died. This led us to conclude that the high frequencies of chromatid breaks increased thus the number of daughter cells exiting the cell cycle after asymmetric chromosome segregation, which is consistent with the reduction of proliferative divisions of neural progenitors and premature neurogenesis observed in *Xlf*−/− embryos.

To further explore the link between asymmetric DNA damage and asymmetric division of neural progenitors, WT embryos at E15.5 were exposed to low dose of ionizing radiation (50 mGy) and cortical slices were analyzed 1 h and 3 h later to determine orientation of the cleavage plane of mitotic RGC irradiated during late S and G2. At this low dose and at this time post-irradiation, the metaphases observed are supposed to contain no more than one radio-induced chromatid break and no radio-induced chromosome break. As shown in Figure S4, the mean of angles formed by the segregation line of daughter chromosomes and the ventricular surface of mitotic RGC was significantly decreased in the irradiated brains as observed above in *Xlf*−/− brains, comforting our hypothesis of a causative role of a single chromatid break in the asymmetric division of neural progenitors.

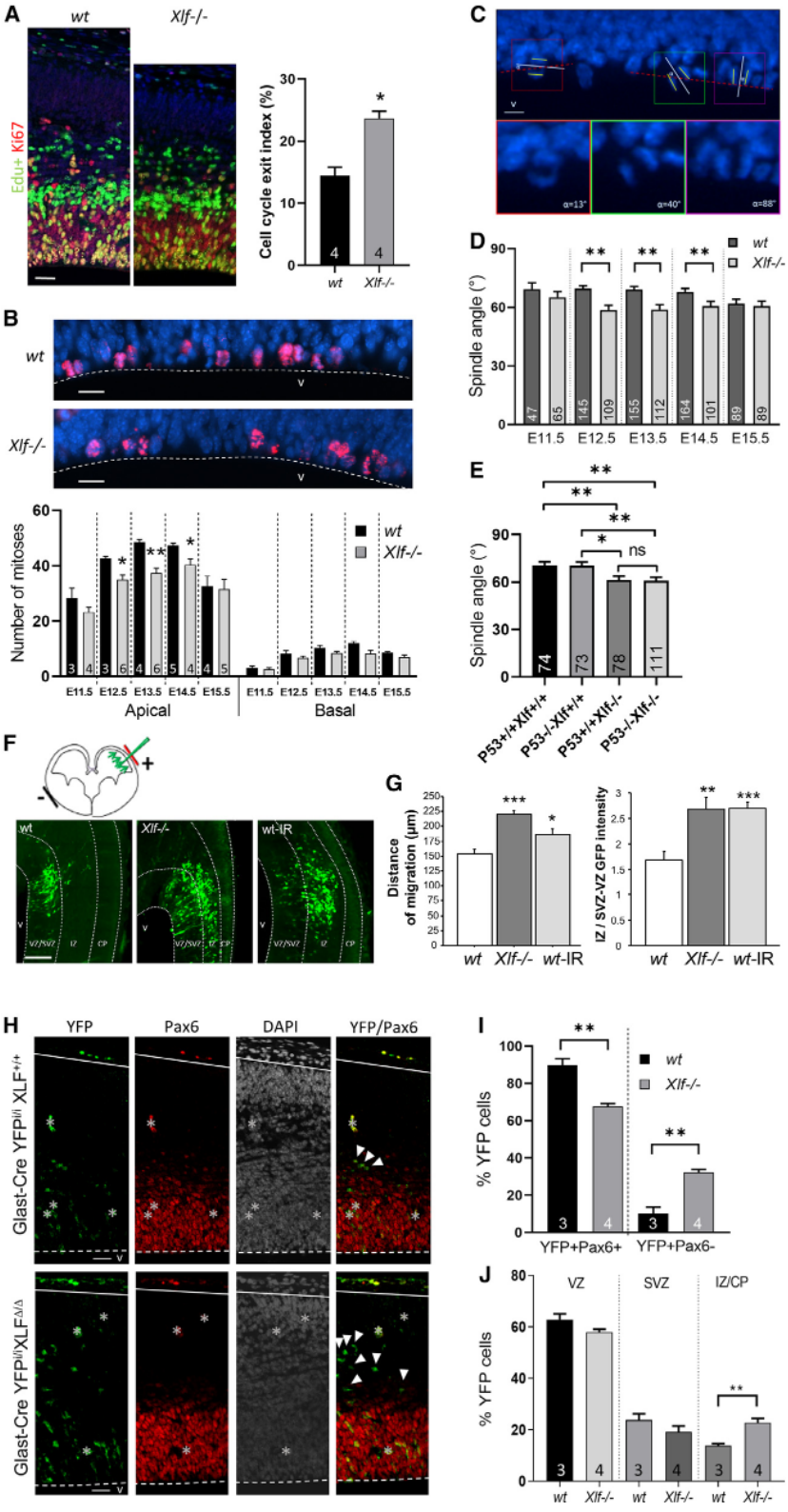

Figure 5. Premature neurogenesis in the brain of *Xlf*−/− embryos

(A) Top: Images of the VZ/SVZ cortices at E15.5, 24 h after EdU labeling and stained for Ki67 (red) and EdU (green). Scale bar, 50 µm. Bottom: Cell cycle exit index calculated as the percentage of EdU-positive cells that were Ki67 negative.[44] For each genotype, four brain slices from four embryo brains were analyzed. Data are mean ± SEM. *p < 0.05. Mann-Whitney test.

(B) Top: Phospho-Histone H3 immunostaining (red) (white dot-line) in coronal slices of WT and *Xlf*−/− embryos at E14.5. V, ventricle. Scale bar, 20 µm. Bottom: Numbers of apical and basal mitoses in the dorsal telencephalon per coronal slice of WT and *Xlf*−/− embryos from E11.5 to E15.5. The numbers of embryos analyzed are given inside the bars.

(C) Method of measurement of RGC mitotic spindle angles. Cleavage planes (white line) were deduced from the orientation of the sister chromatids (short white lines) and the ventricle edge (dashed red line) on coronal cortical slices. The smallest angle between the cleavage plane and the ventricle edge was then calculated. Scale bar, 5 µm. V, ventricle.

(D) Quantification of mitotic spindle angles of apical mitoses in WT and *Xlf*−/− embryos at different developmental stages. They were obtained from three to five embryos. The number of mitoses analyzed (n) are indicated inside the bars. ***p < 0.001, **p < 0.01, *p < 0.05, t test.

(E) Quantification of mitotic spindle angles in *p53*+/+ *Xlf*+/+, *p53*−/−*Xlf*+/+, *p53*+/+*Xlf*−/−, and *p53*−/− *Xlf*−/− embryos.

(F) Migration of WT and *Xlf*−/− eGFP-positive cells after *in utero* electroporation of EGFP-expressing vector in the dorsal telencephalon. On the top, experimental scheme showing the injection vector (green arrows and green needle) into the ventricle of embryonic mice at E13.5 and the orientation of the electrodes (−: anode; +: cathode) during electroporation. On the bottom, detection of EGFP-expressing cells (green) in the dorsal telencephalon of *Xlf*−/− and control WT or 0.5 Gy irradiated (WT-*IR*) embryos 24 h after electroporation. Scale bar, 100 µm. V, ventricle. The dash lines delineate the ventricular edge of the dorsal telencephalon, the VZ/SVZ, IZ, and CP.

(G) On the left, mean maximum distances of migration from the ventricle edge (µm) of EGFP+ cells. n = 6 embryos/group. On the right, mean ratios ± SEM of the EGFP intensity measured in the IZ vs. that measured in the VZ/SVZ. Data have been obtained from six embryos from different litters per group.

(H–J) Glast-CreERT2;*Xlf*$^{fl/fl}$;R26R-YFP and Glast-CreERT2;*Xlf*$^{WT/WT}$;R26R-YFP embryos were treated with tamoxifen at E12.5 and YFP+ cell localization was analyzed in cortical slices at E14.5. (H) Representative fluorescent photomicrographs of brain coronal sections obtained from the dorso-medial cerebral wall from E14.5 embryos stained for Pax6 (red), GFP (green), and DAPI (gray). Blood vessels are masked by *, white arrows: YFP cells. Scale bar, 50 µm. (I) More *Xlf*−/− YFP+ cells have lost Pax6 expression. The bar graph shows the mean percentages ± SEM of YFP+Pax6+ and YFP+Pax6− cells per cortical slice. **p < 0.01, Mann-Whitney test. (J) More *Xlf*−/− YFP+ cells have exited the proliferative zone. The bar graph shows the mean percentages ± SEM of YFP+ WT cells and YFP+ *Xlf*−/− cells detected per cortical slice in the different layers of the dorsal telencephalon.***p < 0.001, **p < 0.01, *p < 0.05, Mann-Whitney test.

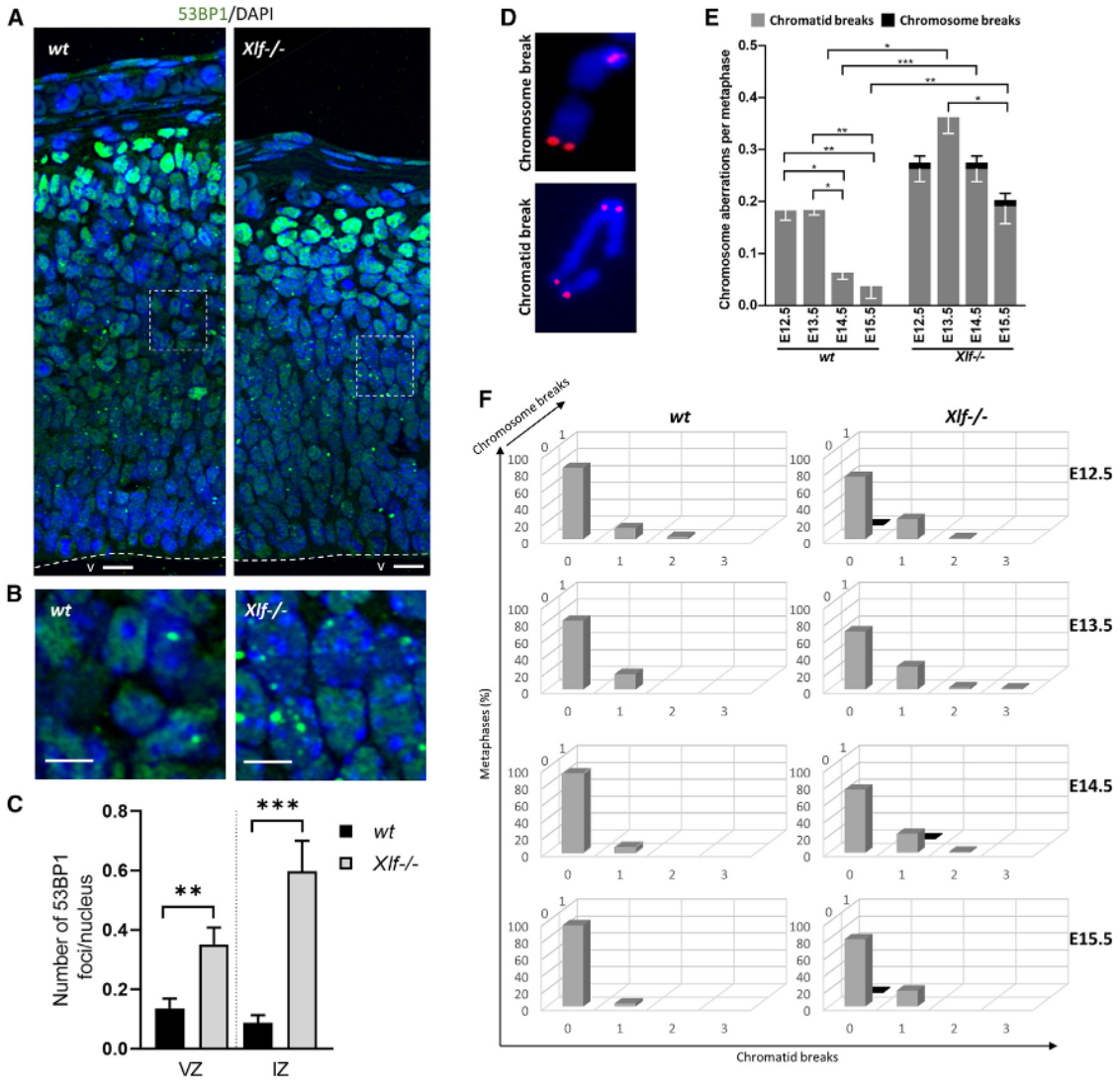

Figure 6. Chromosome instability in cortical WT and *Xlf*−/− neural progenitors during embryonic development

(A) Coronal sections of the cortex of E14.5 WT and *Xlf*−/− embryos stained with DAPI (blue) and antibodies directed against 53BP1 (green). V, ventricle. Scale bar, 20 μm.

(B) Higher magnification as delimited by dotted white box. Scale bar, 10 μm.

(C) Number of 53BP1 foci per nucleus in SVZ and IZ, n: 3 different embryos. ***p < 0.001, **p < 0.01, Mann-Whitney test.

(D) Metaphase spreads were directly prepared from embryonic dorsal telencephalons without any culture step and stained by DAPI and Telo-FISH. Examples of chromatid and chromosome breaks (telomeres in red and DAPI in blue).

(E) Bar graph showing the mean ± SEM number of chromatid and chromosome breaks per metaphase from four embryos. Seventy-six to 80 metaphases from four embryos of two different litters were analyzed. ***p < 0.001, **p < 0.01, *p < 0.05, Mann-Whitney test.

(F) Three-dimensional bar graph showing the distribution of chromatid and chromosome breaks per metaphase.

DISCUSSION

We reported here for the first time that *Xlf* deficiency delayed the fetal cerebral cortex development and the postnatal brain maturation, leading to a mild microcephaly in adult mice. Whereas other causes may not be totally excluded, these neurodevelopmental defects appear to be directly involved in the significant behavioral alterations we observed in adult *Xlf*−/− mice. These observations are clearly reminiscent of clinical and neuropathologic features in humans with mutations in *Xlf/Cernunnos* or in one of the genes encoding the other components of the cNHEJ ligation enzyme complex.[11,13,14] *Xlf*−/− mice represent thus a useful model to investigate the role of *Xlf* and/or cNHEJ in brain development and how DNA damage and/or DNA repair deficiency may cause neurodevelopmental disorders.

In humans, microcephaly is commonly associated with intellectual disability, especially mental retardation.[51] Consistently,

we showed that microcephaly in adult *Xlf*−/− mice is associated with impaired exploratory activity and social behavior, and a depression-like phenotype. The WM and the corpus callosum (CC) were particularly decreased in these mice. The CC is the largest WM tract in the human brain that regulates higher cognition, such as executive function, social interaction, and language.[52,53] Indeed, the CC is composed of fiber bundles that link both hemispheres, hence facilitating the integration of sensorimotor information from the two sides of the body. Consequently, partial CC agenesis and hypoplasia reduce axonal connections between cortical areas known to be involved in behavioral alterations observed in people with autism.[54] Further investigations of the implication of the CC hypoplasia in the cognitive disability of *Xlf*−/− mice should thus provide new mechanistic insight on neurodevelopmental disorders.

We showed that microcephaly in *Xlf*−/− mice is related to several interconnected events that occurred during the embryonic brain development: (1) apoptosis but at a low level, (2) alterations of the neural progenitor pool, consisting essentially in an early decrease in symmetric proliferative divisions leading to premature neurogenesis, and (3) increase in chromosome instability. Neural cells in the developing brain of mouse embryos fully deficient in cNHEJ undergo a massive apoptosis at developmental time points associated with differentiation into postmitotic, mature neurons.[40] Similarly, most apoptotic cells in the *Xlf*−/− embryonic brains were detected outside the germinative zone (VZ and SVZ), indicating that apoptosis occurred mostly after differentiation. Gogendeau and colleagues[55] have shown that premature differentiation is an alternative response of *Drosophila* neural stem cells to prevent aneuploid cells from cycling. Premature differentiation of neural stem cells has also been observed in a mouse model of centrosome amplification causing highly aneuploid cells when apoptosis was inhibited.[56] Furthermore, microcephaly has been shown to arise from a variety of genetic and environmental factors affecting brain development through alterations of neural progenitor divisions.[57–62] We show here that premature differentiation is the key factor reducing the neural progenitor pool and, considering the low level of apoptosis, likely a major cause of microcephaly in *Xlf*−/− embryos. This was further confirmed by the decrease of both the neural progenitor pool and the cortical thickness associated with the increase of asymmetric divisions in *p53*−/−*Xlf*−/− mice, in which apoptosis of neural cells induced by the NHEJ defect is abolished.

Ex vivo analyses of the developing dorsal telencephalon revealed that a high percentage (nearly 18% at early developmental stages) of metaphases of WT cortical neural progenitors contained chromatid breaks. Detection of this particular type of chromosome aberrations reveals that neural progenitors are particularly exposed to DNA damage during late S and/or G2 phase *in vivo*. This is consistent with several reports showing a high rate of recurrent DNA breaks related to replication stress, particularly within large and late replicating genes in cultured NSPCs deficient for cNHEJ.[5,6,40,63–66]

We showed that chromatid breaks were more frequent in metaphases from *Xlf*-deficient mice (detection in more than 30% metaphases). Since XLF has been recently reported to function during DNA replication to prevent the accumulation of reversed replication forks in a manner that is independent of cNHEJ,[67] further experiments should determine the respective involvement of the XLF functions dependent and independent of cNHEJ in the generation of chromatid breaks at metaphase in neural progenitors.

Interestingly, we found a significant decrease in chromatid breaks in WT neural progenitors at late compared with early developmental stages. Since they constantly remained elevated in *Xlf*-deficient mice, their decrease in WT cells cannot be attributed to a decrease of the DNA damage rate with the developmental stage. Rather, this decrease likely results from an XLF-dependent adaptive response of neural progenitors, increasing their DNA repair capacity to the DNA damage rate, as previously reported in cultures of neural progenitors exposed to chronic genotoxic stress.[7]

Based on the observation of the high rate of recurrent DSBs in cultured neural progenitors, it has been suggested that neuronal development may involve genomic alterations and perhaps diversification of genomic information that may be functionally related to the process of antigen receptor rearrangement via V(D)J recombination.[5,40] cNHEJ being known to be error prone, the *Xlf*-dependent adaptive response of neural progenitors to the high rate of DNA damage in the developing cortex may favor the generation of genetically diverse and viable cells. Importantly, it should be noted that the cytogenetic approach used in this study allows the detection of persistent DSBs at metaphase (chromatid breaks and chromosome breaks), but does not allow the detection of faulty DNA repair (such as recombination, inversion, deletion, etc.), except chromatid or chromosome fusions (both of which were not detected here). Further methods should be used to investigate the impact of *Xlf* deletion of the generation of neuronal genetic diversity during brain development.

The very low level of chromosome-type aberrations, as compared with chromatid-type aberrations found in neural progenitor metaphases, clearly showed that WT as well as *Xlf*−/− daughter cells inheriting chromosomes with terminal deletions did not undergo further divisions in the developing cortex. Persistent DSBs being highly toxic, most of these cells likely entered apoptosis after differentiation. In mice fully deficient for cNHEJ (*LigIV*−/−, *Xrcc4*−/−), the high level of unrepaired DSBs reduces the probability to generate cells without any chromosome breaks leading to a massive apoptosis and embryonic lethality. By contrast, most aberrant metaphases from *Xlf*−/− embryos contained only one chromatid break. This potentially allows generating via asymmetric division one daughter cell inheriting a terminally deleted chromosome and another one with a normal karyotype. Therefore, together with apoptosis of daughter cells with the chromosome aberrations, these asymmetric divisions limit, but do not prevent, further cortex development and *Xlf*−/− embryo viability.

Altogether, our results suggest a direct link between the DNA repair defect leading to asymmetric segregation of chromosomes in neural progenitors and the increase of neurogenic divisions in the brain of *Xlf*−/− embryos. In WT mice, coupling asymmetric chromosome segregation with asymmetric neurogenic divisions after faulty repair of DNA breaks related to replication stress may allow both the self-renewal of neural progenitors

and the creation of neuronal genetic diversity during brain development.

It is now well accepted that there are large polymorphisms in DNA repair genes in humans that could influence individual DNA repair capacity.[68–70] Our study clearly identifies a low DNA repair insufficiency as a major cause of neurodevelopmental impairment. Moreover, humans can be more and more exposed to numerous DNA damaging agents (pollutants, ionizing radiation related to nuclear accidents, clinical diagnostic tests such as computed tomography scan, or treatments such as radiotherapy), and the developing brain has been shown to be highly sensitive to genotoxic stress.[71,72] Low-dose exposure to genotoxic agents during pregnancy could thus severely worsen the consequences of a low DNA repair insufficiency on brain development.

Limitations of the study

In this study, we report substantial behavioral alterations in *Xlf*-deficient mice, which are likely caused by the neurodevelopmental impairments we observed in these mice and therefore by the impact of *Xlf* deficiency on neurogenesis. However, we cannot totally exclude the role of immune defect resulting from *Xlf* deficiency, although this defect is slight in *Xlf*−/− mice with a moderate B and T cell lymphopenia and importantly with no alteration of the monocyte/macrophage lineage.[20–23] This question could be thus addressed using brain-specific KO mice.

Apoptosis, a well-known cause of microcephaly, is very low in *Xlf*−/− embryos. Our data suggest therefore that premature neurogenesis plays a major role in the microcephaly related to *Xlf* deficiency by reducing the pool of neural progenitors at early developmental stages. In agreement with this, apoptosis inhibition did not prevent the decrease of both the neural progenitor pool and of the cortical thickness in *p53*−/−*Xlf*−/− embryos at E14.5. The thickness of CP was also decreased, but not to the same extent as in *p53*+/+*Xlf*−/− embryos, suggesting that the low level of apoptosis associated with *Xlf* deficiency may also play a significant role in microcephaly. However, we can also hypothesize that, due to apoptosis inhibition, the higher rate of neuron production resulting from premature neurogenesis contributed to increase the thickness of the CP at E14.5 in *p53*−/−*Xlf*−/− embryos as compared with *p53*+/+*Xlf*−/− embryos. Further study of cortex growth in *p53*−/−*Xlf*−/− mice at later developmental stages could help clarify the respective contribution of premature neurogenesis and apoptosis in microcephaly related to *Xlf* deficiency.

STAR★METHODS

Detailed methods are provided in the online version of this paper and include the following:

- KEY RESOURCES TABLE
- RESOURCE AVAILABILITY
  - Lead contact
  - Materials availability
  - Data and code availability
- EXPERIMENTAL MODEL AND SUBJECT DETAILS
  - Animal care and use
- METHOD DETAILS
  - Mouse genotyping
  - Mouse treatments
  - Sensorimotor testing of mouse pups
  - Behavioral phenotyping of adult mice
  - Magnetic resonance imaging (MRI)
  - Antibodies
  - Histological analysis
  - Chromosome instability
- QUANTIFICATION AND STATISTICAL ANALYSIS
  - Image analysis
- QUANTIFICATION AND STATISTICAL ANALYSES

SUPPLEMENTAL INFORMATION

Supplemental information can be found online at https://doi.org/10.1016/j.celrep.2023.112342.

ACKNOWLEDGMENTS

We are indebted to Véronique Neuville for animal care, Sebastien Messiaen for multiplex immunofluorescence platform, and Denis Biard for providing his pEBV-eGFP vector. This study was supported by grants from Segment Radiobiologie (IRBIO, CEA), Electricité de France (EDF), and ANR (NeuroPest). The study was also supported by funding from the European Union Seventh Framework Programme (FP7/2007-2013) under grant agreement n° 323267 (RISK-IR). MRI analyses were performed on a platform of the "France Life Imaging" network partly funded by the grant "ANR-11-INBS-0006."

AUTHOR CONTRIBUTIONS

A.B. and O.E.: behavioral assays, histopathological analyses, *in utero* electroporation, interpretation of the data, manuscript writing. L.M., F.B., E.A.P., and D.L.B.: IRM analyses and interpretation. T.K.: histopathological analyses. S.M., C.G.-B., and C.D., cytogenetic study. L.R.G.: *in utero* electroporation and histopathological analyses. V.B.: animal crossing and genotyping. J.V., A.L., S.M., A.M.: behavioral assays. V.A.J.-P.V.: generation of mice strains, proposed and discussed experiments. F.D.B.: direction of the study, financing, interpretation of the data, manuscript writing.

DECLARATION OF INTERESTS

The authors declare no competing interests.

Received: December 1, 2020
Revised: December 20, 2022
Accepted: March 19, 2023

REFERENCES

1. McKinnon, P.J. (2013). Maintaining genome stability in the nervous system. Nat. Neurosci. *16*, 1523–1529. https://doi.org/10.1038/nn.3537.
2. Aguilera, A., and García-Muse, T. (2013). Causes of genome instability. Annu. Rev. Genet. *47*, 1–32. https://doi.org/10.1146/annurev-genet-111212-133232.
3. Erwin, J.A., Marchetto, M.C., and Gage, F.H. (2014). Mobile DNA elements in the generation of diversity and complexity in the brain. Nat. Rev. Neurosci. *15*, 497–506. https://doi.org/10.1038/nrn3730.
4. Madabhushi, R., Gao, F., Pfenning, A.R., Pan, L., Yamakawa, S., Seo, J., Rueda, R., Phan, T.X., Yamakawa, H., Pao, P.-C., et al. (2015). Activity-induced DNA breaks govern the expression of neuronal early-response genes. Cell *161*, 1592–1605. https://doi.org/10.1016/j.cell.2015.05.032.

5. Wei, P.-C., Chang, A.N., Kao, J., Du, Z., Meyers, R.M., Alt, F.W., and Schwer, B. (2016). Long neural genes harbor recurrent DNA break clusters in neural stem/progenitor cells. Cell *164*, 644–655. https://doi.org/10.1016/j.cell.2015.12.039.

6. Wei, P.-C., Lee, C.-S., Du, Z., Schwer, B., Zhang, Y., Kao, J., Zurita, J., and Alt, F.W. (2018). Three classes of recurrent DNA break clusters in brain progenitors identified by 3D proximity-based break joining assay. Proc. Natl. Acad. Sci. USA *115*, 1919–1924. https://doi.org/10.1073/pnas.1719907115.

7. Mokrani, S., Granotier-Beckers, C., Etienne, O., Kortulewski, T., Grisolia, C., de Villartay, J.-P., and Boussin, F.D. (2020). Higher chromosome stability in embryonic neural stem and progenitor cells than in fibroblasts in response to acute or chronic genotoxic stress. DNA Repair *88*, 102801. https://doi.org/10.1016/j.dnarep.2020.102801.

8. Ahnesorg, P., Smith, P., and Jackson, S.P. (2006). XLF interacts with the XRCC4-DNA ligase IV complex to promote DNA nonhomologous end-joining. Cell *124*, 301–313. https://doi.org/10.1016/j.cell.2005.12.031.

9. Buck, D., Malivert, L., de Chasseval, R., Barraud, A., Fondanèche, M.C., Sanal, O., Plebani, A., Stéphan, J.L., Hufnagel, M., le Deist, F., et al. (2006). Cernunnos, a novel nonhomologous end-joining factor, is mutated in human immunodeficiency with microcephaly. Cell *124*, 287–299. https://doi.org/10.1016/j.cell.2005.12.030.

10. Moshous, D., Callebaut, I., de Chasseval, R., Corneo, B., Cavazzana-Calvo, M., Le Deist, F., Tezcan, I., Sanal, O., Bertrand, Y., Philippe, N., et al. (2001). Artemis, a novel DNA double-strand break repair/V(D)J recombination protein, is mutated in human severe combined immune deficiency. Cell *105*, 177–186. https://doi.org/10.1016/S0092-8674(01)00309-9.

11. Woodbine, L., Neal, J.A., Sasi, N.-K., Shimada, M., Deem, K., Coleman, H., Dobyns, W.B., Ogi, T., Meek, K., Davies, E.G., and Jeggo, P.A. (2013). PRKDC mutations in a SCID patient with profound neurological abnormalities. J. Clin. Invest. *123*, 2969–2980. https://doi.org/10.1172/JCI67349.

12. O'Driscoll, M., Cerosaletti, K.M., Girard, P.M., Dai, Y., Stumm, M., Kysela, B., Hirsch, B., Gennery, A., Palmer, S.E., Seidel, J., et al. (2001). DNA ligase IV mutations identified in patients exhibiting developmental delay and immunodeficiency. Mol. Cell *8*, 1175–1185. https://doi.org/10.1016/s1097-2765(01)00408-7.

13. Altmann, T., and Gennery, A.R. (2016). DNA ligase IV syndrome; a review. Orphanet J. Rare Dis. *11*, 137. https://doi.org/10.1186/s13023-016-0520-1.

14. de Villartay, J.-P. (2015). When natural mutants do not fit our expectations: the intriguing case of patients with XRCC4 mutations revealed by whole-exome sequencing. EMBO Mol. Med. *7*, 862–864. https://doi.org/10.15252/emmm.201505307.

15. Gao, Y., Sun, Y., Frank, K.M., Dikkes, P., Fujiwara, Y., Seidl, K.J., Sekiguchi, J.M., Rathbun, G.A., Swat, W., Wang, J., et al. (1998). A critical role for DNA end-joining proteins in both lymphogenesis and neurogenesis. Cell *95*, 891–902. https://doi.org/10.1016/s0092-8674(00)81714-6.

16. Barnes, D.E., Stamp, G., Rosewell, I., Denzel, A., and Lindahl, T. (1998). Targeted disruption of the gene encoding DNA ligase IV leads to lethality in embryonic mice. Curr. Biol. *8*, 1395–1398. https://doi.org/10.1016/s0960-9822(98)00021-9.

17. Frank, K.M., Sekiguchi, J.M., Seidl, K.J., Swat, W., Rathbun, G.A., Cheng, H.L., Davidson, L., Kangaloo, L., and Alt, F.W. (1998). Late embryonic lethality and impaired V(D)J recombination in mice lacking DNA ligase IV. Nature *396*, 173–177. https://doi.org/10.1038/24172.

18. Dai, Y., Kysela, B., Hanakahi, L.A., Manolis, K., Riballo, E., Stumm, M., Harville, T.O., West, S.C., Oettinger, M.A., and Jeggo, P.A. (2003). Nonhomologous end joining and V(D)J recombination require an additional factor. Proc. Natl. Acad. Sci. USA *100*, 2462–2467. https://doi.org/10.1073/pnas.0437964100.

19. Abramowski, V., Etienne, O., Elsaid, R., Yang, J., Berland, A., Kermasson, L., Roch, B., Musilli, S., Moussu, J.-P., Lipson-Ruffert, K., et al. (2018). PAXX and Xlf interplay revealed by impaired CNS development and immunodeficiency of double KO mice. Cell Death Differ. *25*, 444–452. https://doi.org/10.1038/cdd.2017.184.

20. Li, G., Alt, F.W., Cheng, H.-L., Brush, J.W., Goff, P.H., Murphy, M.M., Franco, S., Zhang, Y., and Zha, S. (2008). Lymphocyte-specific compensation for XLF/cernunnos end-joining functions in V(D)J recombination. Mol. Cell *31*, 631–640. https://doi.org/10.1016/j.molcel.2008.07.017.

21. Vera, G., Rivera-Munoz, P., Abramowski, V., Malivert, L., Lim, A., Bole-Feysot, C., Martin, C., Florkin, B., Latour, S., Revy, P., and de Villartay, J.P. (2013). Cernunnos deficiency reduces thymocyte life span and alters the T cell repertoire in mice and humans. Mol. Cell Biol. *33*, 701–711. https://doi.org/10.1128/MCB.01057-12.

22. Roch, B., Abramowski, V., Chaumeil, J., and de Villartay, J.-P. (2019). Cernunnos/xlf deficiency results in Suboptimal V(D)J recombination and impaired lymphoid development in mice. Front. Immunol. *10*, 443. https://doi.org/10.3389/fimmu.2019.00443.

23. Musilli, S., Abramowski, V., Roch, B., and de Villartay, J.-P. (2020). An in vivo study of the impact of deficiency in the DNA repair proteins PAXX and XLF on development and maturation of the hemolymphoid system. J. Biol. Chem. *295*, 2398–2406. https://doi.org/10.1074/jbc.AC119.010924.

24. Zha, S., Guo, C., Boboila, C., Oksenych, V., Cheng, H.-L., Zhang, Y., Wesemann, D.R., Yuen, G., Patel, H., Goff, P.H., et al. (2011). ATM damage response and XLF repair factor are functionally redundant in joining DNA breaks. Nature *469*, 250–254. https://doi.org/10.1038/nature09604.

25. Lescale, C., Lenden Hasse, H., Blackford, A.N., Balmus, G., Bianchi, J.J., Yu, W., Bacoccina, L., Jarade, A., Clouin, C., Sivapalan, R., et al. (2016). Specific roles of XRCC4 Paralogs PAXX and XLF during V(D)J recombination. Cell Rep. *16*, 2967–2979. https://doi.org/10.1016/j.celrep.2016.08.069.

26. Balmus, G., Barros, A.C., Wijnhoven, P.W.G., Lescale, C., Hasse, H.L., Boroviak, K., le Sage, C., Doe, B., Speak, A.O., Galli, A., et al. (2016). Synthetic lethality between PAXX and XLF in mammalian development. Genes Dev. *30*, 2152–2157. https://doi.org/10.1101/gad.290510.116.

27. Liu, X., Shao, Z., Jiang, W., Lee, B.J., and Zha, S. (2017). PAXX promotes KU accumulation at DNA breaks and is essential for end-joining in XLF-deficient mice. Nat. Commun. *8*, 13816–13913. https://doi.org/10.1038/ncomms13816.

28. van Tilborg, E., van Kammen, C.M., de Theije, C.G.M., van Meer, M.P.A., Dijkhuizen, R.M., and Nijboer, C.H. (2017). A quantitative method for microstructural analysis of myelinated axons in the injured rodent brain. Sci. Rep. *7*, 16492. https://doi.org/10.1038/s41598-017-16797-1.

29. Holmes, A. (2001). Targeted gene mutation approaches to the study of anxiety-like behavior in mice. Neurosci. Biobehav. Rev. *25*, 261–273. https://doi.org/10.1016/s0149-7634(01)00012-4.

30. Brooks, S.P., and Dunnett, S.B. (2009). Tests to assess motor phenotype in mice: a user's guide. Nat. Rev. Neurosci. *10*, 519–529. https://doi.org/10.1038/nrn2652.

31. Can, A., Dao, D.T., Arad, M., Terrillion, C.E., Piantadosi, S.C., and Gould, T.D. (2011). The mouse forced swim test. J. Vis. Exp., e3638. https://doi.org/10.3791/3638.

32. Leger, M., Quiedeville, A., Bouet, V., Haelewyn, B., Boulouard, M., Schumann-Bard, P., and Freret, T. (2013). Object recognition test in mice. Nat. Protoc. *8*, 2531–2537. https://doi.org/10.1038/nprot.2013.155.

33. Mamiya, T., and Ukai, M. (2001). [Gly(14)]-Humanin improved the learning and memory impairment induced by scopolamine in vivo. Br. J. Pharmacol. *134*, 1597–1599. https://doi.org/10.1038/sj.bjp.0704429.

34. Silverman, J.L., Yang, M., Lord, C., and Crawley, J.N. (2010). Behavioural phenotyping assays for mouse models of autism. Nat. Rev. Neurosci. *11*, 490–502. https://doi.org/10.1038/nrn2851.

35. Moy, S.S., Nadler, J.J., Perez, A., Barbaro, R.P., Johns, J.M., Magnuson, T.R., Piven, J., and Crawley, J.N. (2004). Sociability and preference for social novelty in five inbred strains: an approach to assess autistic-like

behavior in mice. Genes Brain Behav. *3*, 287–302. https://doi.org/10.1111/j.1601-1848.2004.00076.x.

36. Noctor, S.C., Martínez-Cerdeño, V., Ivic, L., and Kriegstein, A.R. (2004). Cortical neurons arise in symmetric and asymmetric division zones and migrate through specific phases. Nat. Neurosci. *7*, 136–144. https://doi.org/10.1038/nn1172.
37. Götz, M., and Huttner, W.B. (2005). The cell biology of neurogenesis. Nat. Rev. Mol. Cell Biol. *6*, 777–788. https://doi.org/10.1038/nrm1739.
38. Englund, C., Fink, A., Lau, C., Pham, D., Daza, R.A.M., Bulfone, A., Kowalczyk, T., and Hevner, R.F. (2005). Pax6, Tbr2, and Tbr1 are expressed sequentially by radial glia, intermediate progenitor cells, and postmitotic neurons in developing neocortex. J. Neurosci. *25*, 247–251. https://doi.org/10.1523/JNEUROSCI.2899-04.2005.
39. Orii, K.E., Lee, Y., Kondo, N., and McKinnon, P.J. (2006). Selective utilization of nonhomologous end-joining and homologous recombination DNA repair pathways during nervous system development. Proc. Natl. Acad. Sci. USA *103*, 10017–10022. https://doi.org/10.1073/pnas.0602436103.
40. Alt, F.W., and Schwer, B. (2018). DNA double-strand breaks as drivers of neural genomic change, function, and disease. DNA Repair *71*, 158–163. https://doi.org/10.1016/j.dnarep.2018.08.019.
41. Roque, T., Haton, C., Etienne, O., Chicheportiche, A., Rousseau, L., Martin, L., Mouthon, M.-A., and Boussin, F.D. (2012). Lack of a p21waf1/cip -dependent G1/S checkpoint in neural stem and progenitor cells after DNA damage in vivo. Stem Cell. *30*, 537–547. https://doi.org/10.1002/stem.1010.
42. Frank, K.M., Sharpless, N.E., Gao, Y., Sekiguchi, J.M., Ferguson, D.O., Zhu, C., Manis, J.P., Horner, J., DePinho, R.A., and Alt, F.W. (2000). DNA ligase IV deficiency in mice leads to defective neurogenesis and embryonic lethality via the p53 pathway. Mol. Cell *5*, 993–1002. https://doi.org/10.1016/s1097-2765(00)80264-6.
43. Gao, Y., Ferguson, D.O., Xie, W., Manis, J.P., Sekiguchi, J., Frank, K.M., Chaudhuri, J., Horner, J., DePinho, R.A., and Alt, F.W. (2000). Interplay of p53 and DNA-repair protein XRCC4 in tumorigenesis, genomic stability and development. Nature *404*, 897–900. https://doi.org/10.1038/35009138.
44. Xu, D., Zhang, F., Wang, Y., Sun, Y., and Xu, Z. (2014). Microcephaly-associated protein WDR62 regulates neurogenesis through JNK1 in the developing neocortex. Cell Rep. *6*, 104–116. https://doi.org/10.1016/j.celrep.2013.12.016.
45. Sun, T., and Hevner, R.F. (2014). Growth and folding of the mammalian cerebral cortex: from molecules to malformations. Nat. Rev. Neurosci. *15*, 217–232. https://doi.org/10.1038/nrn3707.
46. Gauthier-Fisher, A., Lin, D.C., Greeve, M., Kaplan, D.R., Rottapel, R., and Miller, F.D. (2009). Lfc and Tctex-1 regulate the genesis of neurons from cortical precursor cells. Nat. Neurosci. *12*, 735–744. https://doi.org/10.1038/nn.2339.
47. Konno, D., Shioi, G., Shitamukai, A., Mori, A., Kiyonari, H., Miyata, T., and Matsuzaki, F. (2008). Neuroepithelial progenitors undergo LGN-dependent planar divisions to maintain self-renewability during mammalian neurogenesis. Nat. Cell Biol. *10*, 93–101. https://doi.org/10.1038/ncb1673.
48. Etienne, O., Roque, T., Haton, C., and Boussin, F.D. (2012). Variation of radiation-sensitivity of neural stem and progenitor cell populations within the developing mouse brain. Int. J. Radiat. Biol. *88*, 694–702. https://doi.org/10.3109/09553002.2012.710927.
49. Shimogori, T., and Ogawa, M. (2008). Gene application with in utero electroporation in mouse embryonic brain. Dev. Growth Differ. *50*, 499–506. https://doi.org/10.1111/j.1440-169X.2008.01045.x.
50. Hladik, D., and Tapio, S. (2016). Effects of ionizing radiation on the mammalian brain. Mutat. Res. Rev. Mutat. Res. *770*, 219–230. https://doi.org/10.1016/j.mrrev.2016.08.003.
51. Watemberg, N., Silver, S., Harel, S., and Lerman-Sagie, T. (2002). Significance of microcephaly Among children with developmental disabilities. J. Child Neurol. *17*, 117–122. https://doi.org/10.1177/088307380201700205.
52. Highley, J.R., Esiri, M.M., McDonald, B., Cortina-Borja, M., Herron, B.M., and Crow, T.J. (1999). The size and fibre composition of the corpus callosum with respect to gender and schizophrenia: a post-mortem study. Brain *122*, 99–110. https://doi.org/10.1093/brain/122.1.99.
53. Riise, J., and Pakkenberg, B. (2011). Stereological estimation of the total number of myelinated callosal fibers in human subjects. J. Anat. *218*, 277–284. https://doi.org/10.1111/j.1469-7580.2010.01333.x.
54. Wegiel, J., Flory, M., Kaczmarski, W., Brown, W.T., Chadman, K., Wisniewski, T., Nowicki, K., Kuchna, I., Ma, S.Y., and Wegiel, J. (2017). Partial agenesis and hypoplasia of the corpus callosum in idiopathic autism. J. Neuropathol. Exp. Neurol. *76*, 225–237. https://doi.org/10.1093/jnen/nlx003.
55. Gogendeau, D., Siudeja, K., Gambarotto, D., Pennetier, C., Bardin, A.J., and Basto, R. (2015). Aneuploidy causes premature differentiation of neural and intestinal stem cells. Nat. Commun. *6*, 8894. https://doi.org/10.1038/ncomms9894.
56. Marthiens, V., Rujano, M.A., Pennetier, C., Tessier, S., Paul-Gilloteaux, P., and Basto, R. (2013). Centrosome amplification causes microcephaly. Nat. Cell Biol. *15*, 731–740. https://doi.org/10.1038/ncb2746.
57. Gruber, R., Zhou, Z., Sukchev, M., Joerss, T., Frappart, P.-O., and Wang, Z.-Q. (2011). MCPH1 regulates the neuroprogenitor division mode by coupling the centrosomal cycle with mitotic entry through the Chk1–Cdc25 pathway. Nat. Cell Biol. *13*, 1325–1334. https://doi.org/10.1038/ncb2342.
58. Barrera, J.A., Kao, L.-R., Hammer, R.E., Seemann, J., Fuchs, J.L., and Megraw, T.L. (2010). CDK5RAP2 regulates centriole engagement and cohesion in mice. Dev. Cell *18*, 913–926. https://doi.org/10.1016/j.devcel.2010.05.017.
59. Chen, J.-F., Zhang, Y., Wilde, J., Hansen, K.C., Lai, F., and Niswander, L. (2014). Microcephaly disease gene Wdr62 regulates mitotic progression of embryonic neural stem cells and brain size. Nat. Commun. *5*, 3885. https://doi.org/10.1038/ncomms4885.
60. Jayaraman, D., Kodani, A., Gonzalez, D.M., Mancias, J.D., Mochida, G.H., Vagnoni, C., Johnson, J., Krogan, N., Harper, J.W., Reiter, J.F., et al. (2016). Microcephaly proteins Wdr62 and Aspm define a mother centriole complex regulating centriole biogenesis, apical complex, and cell fate. Neuron *92*, 813–828. https://doi.org/10.1016/j.neuron.2016.09.056.
61. Sgourdou, P., Mishra-Gorur, K., Saotome, I., Henagariu, O., Tuysuz, B., Campos, C., Ishigame, K., Giannikou, K., Quon, J.L., Sestan, N., et al. (2017). Disruptions in asymmetric centrosome inheritance and WDR62-Aurora kinase B interactions in primary microcephaly. Sci. Rep. *7*, 43708. https://doi.org/10.1038/srep43708.
62. Merfeld, E., Ben-Avi, L., Kennon, M., and Cerveny, K.L. (2017). Potential mechanisms of Zika-linked microcephaly: Zika-linked microcephaly. Wiley Interdiscip. Rev. Dev. Biol. *6*, e273. https://doi.org/10.1002/wdev.273.
63. Alt, F.W., Wei, P.-C., and Schwer, B. (2017). Recurrently breaking genes in neural progenitors: Potential roles of DNA breaks in neuronal function, degeneration and cancer. In Genome Editing in Neurosciences, R. Jaenisch, F. Zhang, and F. Gage, eds. (Springer).
64. Schwer, B., Wei, P.-C., Chang, A.N., Kao, J., Du, Z., Meyers, R.M., and Alt, F.W. (2016). Transcription-associated processes cause DNA double-strand breaks and translocations in neural stem/progenitor cells. Proc. Natl. Acad. Sci. USA *113*, 2258–2263. https://doi.org/10.1073/pnas.1525564113.
65. Wang, M., Wei, P.-C., Lim, C.K., Gallina, I.S., Marshall, S., Marchetto, M.C., Alt, F.W., and Gage, F.H. (2020). Increased neural progenitor proliferation in a hiPSC model of autism induces replication stress-associated genome instability. Cell Stem Cell *26*, 221–233.e6. https://doi.org/10.1016/j.stem.2019.12.013.
66. Tena, A., Zhang, Y., Kyritsis, N., Devorak, A., Zurita, J., Wei, P.-C., and Alt, F.W. (2020). Induction of recurrent break cluster genes in neural progenitor

cells differentiated from embryonic stem cells in culture. Proc. Natl. Acad. Sci. USA *117*, 10541–10546. https://doi.org/10.1073/pnas.1922299117.

67. Chen, B.-R., Quinet, A., Byrum, A.K., Jackson, J., Berti, M., Thangavel, S., Bredemeyer, A.L., Hindi, I., Mosammaparast, N., Tyler, J.K., et al. (2019). XLF and H2AX function in series to promote replication fork stability. J. Cell Biol. *218*, 2113–2123. https://doi.org/10.1083/jcb.201808134.
68. Cornetta, T., Festa, F., Testa, A., and Cozzi, R. (2006). DNA damage repair and genetic polymorphisms: assessment of individual sensitivity and repair capacity. Int. J. Radiat. Oncol. Biol. Phys. *66*, 537–545. https://doi.org/10.1016/j.ijrobp.2006.06.037.
69. Travis, L.B., Rabkin, C.S., Brown, L.M., Allan, J.M., Alter, B.P., Ambrosone, C.B., Begg, C.B., Caporaso, N., Chanock, S., DeMichele, A., et al. (2006). Cancer survivorship–genetic susceptibility and second primary cancers: research strategies and recommendations. J. Natl. Cancer Inst. *98*, 15–25. https://doi.org/10.1093/jnci/djj001.
70. Mumbrekar, K.D., Goutham, H.V., Vadhiraja, B.M., and Bola Sadashiva, S.R. (2016). Polymorphisms in double strand break repair related genes influence radiosensitivity phenotype in lymphocytes from healthy individuals. DNA Repair *40*, 27–34. https://doi.org/10.1016/j.dnarep.2016.02.006.
71. Nowak, E., Etienne, O., Millet, P., Lages, C.S., Mathieu, C., Mouthon, M.-A., and Boussin, F.D. (2006). Radiation-induced H2AX phosphorylation and neural precursor apoptosis in the developing brain of mice. Radiat. Res. *165*, 155–164. https://doi.org/10.1667/rr3496.1.
72. Verreet, T., Quintens, R., Van Dam, D., Verslegers, M., Tanori, M., Casciati, A., Neefs, M., Leysen, L., Michaux, A., Janssen, A., et al. (2015). A multidisciplinary approach unravels early and persistent effects of X-ray exposure at the onset of prenatal neurogenesis. J. Neurodev. Disord. *7*, 3. https://doi.org/10.1186/1866-1955-7-3.
73. Jacks, T., Remington, L., Williams, B.O., Schmitt, E.M., Halachmi, S., Bronson, R.T., and Weinberg, R.A. (1994). Tumor spectrum analysis in p53-mutant mice. Curr. Biol. *4*, 1–7. https://doi.org/10.1016/s0960-9822(00)00002-6.
74. Ashburner, J., and Friston, K.J. (2005). Unified segmentation. Neuroimage *26*, 839–851. https://doi.org/10.1016/j.neuroimage.2005.02.018.
75. Jenkinson, M., and Smith, S. (2001). A global optimisation method for robust affine registration of brain images. Med. Image Anal. *5*, 143–156.
76. Jenkinson, M., Bannister, P., Brady, M., and Smith, S. (2002). Improved optimization for the robust and Accurate linear registration and motion correction of brain images. Neuroimage *17*, 825–841. https://doi.org/10.1006/nimg.2002.1132.
77. Ferent, J., Cochard, L., Faure, H., Taddei, M., Hahn, H., Ruat, M., and Traiffort, E. (2014). Genetic activation of Hedgehog signaling unbalances the rate of neural stem cell renewal by increasing symmetric divisions. Stem Cell Rep. *3*, 312–323. https://doi.org/10.1016/j.stemcr.2014.05.016.
78. Fox, W.M. (1965). Reflex-ontogeny and behavioural developement of the mouse. Anim. Behav. *13*, 234–241.
79. Roubertoux, P.L., Ghata, A., and Carlier, M. (2018). Measuring Preweaning sensorial and motor development in the mouse: Preweaning development in the mouse. Curr. Protoc. Mouse Biol. *8*, 54–78. https://doi.org/10.1002/cpmo.41.
80. Motz, B.A., and Alberts, J.R. (2005). The validity and utility of geotaxis in young rodents. Neurotoxicol. Teratol. *27*, 529–533.
81. Holmes, A., Hollon, T.R., Gleason, T.C., Liu, Z., Dreiling, J., Sibley, D.R., and Crawley, J.N. (2001). Behavioral characterization of dopamine D5 receptor null mutant mice. Behav. Neurosci. *115*, 1129–1144.
82. Sarnyai, Z., Sibille, E.L., Pavlides, C., Fenster, R.J., McEwen, B.S., and Toth, M. (2000). Impaired hippocampal-dependent learning and functional abnormalities in the hippocampus in mice lacking serotonin(1A) receptors. Proc. Natl. Acad. Sci. USA *97*, 14731–14736. https://doi.org/10.1073/pnas.97.26.14731.
83. Bohlen, M., Cameron, A., Metten, P., Crabbe, J.C., and Wahlsten, D. (2009). Calibration of rotational acceleration for the rotarod test of rodent motor coordination. J. Neurosci. Methods *178*, 10–14. https://doi.org/10.1016/j.jneumeth.2008.11.001.
84. Barrière, D.A., Magalhães, R., Novais, A., Marques, P., Selingue, E., Geffroy, F., Marques, F., Cerqueira, J., Sousa, J.C., Boumezbeur, F., et al. (2019). The SIGMA rat brain templates and atlases for multimodal MRI data analysis and visualization. Nat. Commun. *10*, 5699. https://doi.org/10.1038/s41467-019-13575-7.
85. Godin, J.D., Colombo, K., Molina-Calavita, M., Keryer, G., Zala, D., Charrin, B.C., Dietrich, P., Volvert, M.-L., Guillemot, F., Dragatsis, I., et al. (2010). Huntingtin is required for mitotic spindle orientation and mammalian neurogenesis. Neuron *67*, 392–406. https://doi.org/10.1016/j.neuron.2010.06.027.
86. Rousseau, L., Etienne, O., Roque, T., Desmaze, C., Haton, C., Mouthon, M.-A., Bernardino-Sgherri, J., Essers, J., Kanaar, R., and Boussin, F.D. (2012). In vivo importance of homologous recombination DNA repair for mouse neural stem and progenitor cells. PLoS One *7*, e37194. https://doi.org/10.1371/journal.pone.0037194.
87. Gauthier, L.R., Granotier, C., Hoffschir, F., Etienne, O., Ayouaz, A., Desmaze, C., Mailliet, P., Biard, D.S., and Boussin, F.D. (2012). Rad51 and DNA-PKcs are involved in the generation of specific telomere aberrations induced by the quadruplex ligand 360A that impair mitotic cell progression and lead to cell death. Cell. Mol. Life Sci. *69*, 629–640. https://doi.org/10.1007/s00018-011-0767-6.

STAR★METHODS

KEY RESOURCES TABLE

REAGENT or RESOURCE	SOURCE	IDENTIFIER
Antibodies		
Rabbit anti-Pax6	Cell Signaling	Cat# 60433; RRID:AB_2797599
Mouse anti-βIII	Biolegend	Cat# 801202; RRID:AB_2728521
Rabbit anti-cleaved-caspase 3	Cell Signaling	Cat# 9661; RRID:AB_2341188
Mouse anti-Ki67	BD	Cat# 550609; RRID:AB_393778
Mouse anti-phospho H3	Cell Signaling	Cat# 9606S; RRID:AB_331235
Chicken anti-GFP	Novus	Cat# NB100-1614; RRID:AB_10001164
Mouse anti-BrdU	Roche	Cat# 11170376001; RRID:AB_514483
Rabbit anti-Cux1	Proteintech	Cat# 11733-1-AP; RRID:AB_2086995
Rabbit anti-Bcl11b/Ctip2	Proteintech	Cat# 55414-1-AP; RRID:AB_11182609
Chicken anti-MBP	Millipore	Cat# AB9348; RRID:AB_11213157
Rabbit anti-53PB1	Novus	Cat# NB100-304; RRID:AB_10003037
Rabbit anti-Olig2	Proteintech	Cat# 13999-1-AP; RRID:AB_2157541
Mouse anti-CC1	Abcam	Cat# ab16794; RRID:AB_443473
Goat anti-rabbit Alexa Fluor 488	Thermo Fisher Scientific	Cat# A11008; RRID:AB_143165
Goat anti-rabbit Alexa Fluor 594	Thermo Fisher Scientific	Cat# A11037; RRID:AB_2534095
Goat anti-chicken Alexa Fluor 488	Thermo Fisher Scientific	Cat# A11039; RRID:AB_2534096
Goat anti-chicken Alexa Fluor 647	Thermo Fisher Scientific	Cat# A21449; RRID:AB_2535866
Goat anti-mouse Alexa Fluor 594	Thermo Fisher Scientific	Cat# A11005; RRID:AB_2534073
Experimental models: Organisms/strains		
Mouse: C57BL/6N	Charles river	027C57BL/6
Mouse: Xlf−/−	Jean-Pierre de Villartay	Vera et al. 2013[21]
Mouse: Xlf floxed mice	Jean-Pierre de Villartay	Vera et al. 2013[21]
Mouse: P53−/−	Weinberg, R.A	Jacks et al. 1994[73]
Recombinant DNA		
pEBVCAGeGFP-Bsd	Denis Biard	N/A
Software		
EthoVision 15.0	Noldus	RRID:SCR_000441
NIS-Elements	Nikon Corp	RRID:SCR_014329
ImageJ 1.53k	https://imagej.nih.gov/	RRID:SCR_003070
Metafer	Metasystems	RRID:SCR_016306
Prism 8.1.2	GraphPad	RRID:SCR_002798
SPM	Ashburner and Friston 2005[74]	https://www.fil.ion.ucl.ac.uk/spm/
ITK-Snap	Jenkinson et al. 2001[75]	www.itksnap.org
FSL	Jenkinson et al. 2002[76]	https://fsl.fmrib.ox.ac.uk/fsl/fslwiki/

RESOURCE AVAILABILITY

Lead contact

Further information and requests for resources and reagents should be directed to and will be fulfilled by the lead contact, François D. Boussin (francois.boussin@cea.fr).

Materials availability

This study did not generate new unique reagents.

Data and code availability

- All data reported in this paper will be shared by the lead contact upon request.
- No original code has been generated.
- Any additional information required to reanalyze the data reported in this paper is available from the lead contact upon request.

EXPERIMENTAL MODEL AND SUBJECT DETAILS

Animal care and use

Mouse experiments were carried out in compliance with the European Communities Council Directive of 22th September 2010 (EC/2010/63) and were approved by our institutional committee on animal welfare (authorizations APAFIS#15603-2018060511221 v2, #15631-2018062210374296 v3, #15867-2018070509553060 v1 and 1909-2015091711275868 v1; CEtEA-CEA DRF IdF). Mice were housed in the animal facility of CEA/DRF/IBFJ/iRCM. They were maintained up to five per cage with ad libitum access to food and water at a constant temperature (19–22°C) and humidity (40–50%) on a 12:12-hour light/dark cycle.

Studies on *Xlf*-/- mice[21] and *wt* controls in a C57Bl/6N background were performed on embryos from E11.5 to E15.5 and pups from 3 to 10 days after birth. Sex of embryos and pups were not determined. Only males were used for adult studies.

To obtain *p53*-/-*Xlf*-/- embryos and controls (*p53*-/-*Xlf*+/+, *p53*+/+*Xlf*-/- *and p53*+/+*Xlf*+/+ embryos) at E14.5, *Xlf*-/- mice were crossed with *p53*-/- mice[73] in a mixed genetic background of 129/Sv and C57Bl/6 for 3 generations.

The *Xlf* floxed mice (B6.129-IR847/ICS) that present loxP sites on either side of *Xlf* exon 4[21] were engineered by the Mouse Clinical Institute (MCI; Illkirch, France). They were crossed with Glast-CreERT2/R26R-YFP transgenic mice[77] kindly given by M. Ruat to generate Glast-CreERT2/R26R-YFP/*Xlf*$^{flox/flox}$ mice, which were compared with Glast-CreERT2/R26R-YFP/*Xlf*+/+ control mice. All animals included in this study were heterozygous for (Cre/+) and homozygous for YFP insertion. For embryonic induction of Cre activity, 3 mg of tamoxifen was administrated per mouse by oral gavage of pregnant mice at E12.5 and embryos were analyzed at E14.5. To this end Tamoxifen (Sigma, T5648) was dissolved in corn oil (Sigma, C8267) at 37°C for several hours at 20 mg/ml.

METHOD DETAILS

Mouse genotyping

Mouse tail DNA was used for PCR genotyping. Primer sequences used for GLAST-CreERT2 genotyping were GLAST F8 (5′-GAGG CACTTGGCTAGGCTCTGAGGA-3′), GLAST R3 (5′-GAGGAGATCCTGACCGATCAGTTGG-3′) and CER1 (5‘-GGTGTACGGTCAG TAAATTGGACAT-3′) to amplify a 700-bp product for the wild-type allele and a 400-bp product for the Cre transgene. YFP insertion was determined using 3 primers: R1 (5′-AAAGTCGCTCTGAGTTGTTAT-3′), R2 (5′- GCGAAGAGTTTGTCCTCAACC-3′) and R3 (5′-GCGAAGAGTTTGTCCTCAACC-3′) to amplify a 314 bp product for YFP insertion. Forward primer (2244) 5′-CCTATGGAGCCAG GAGAGAATGC-3′ and reverse primer (2225) 5′-CCTAGGCTCTCAAGAGGAGGG-3′ were used to detect a 316-bp product for the floxed *Xlf* allele and a 266-bp product for the wild-type allele.

Mouse treatments

For cell cycle exit experiments, mice were intraperitoneally injected with EdU (50 mg/kg) at E14.5, sacrificed, and fixed 24 h later.

In utero electroporations were performed as described by Shimogori and Ogawa[49] with few modifications. Pregnant mice (E13.5) were anesthetized with isoflurane gas (Temsega). Both uterine horns containing E13.5 mouse embryos were taken out. One to 1.5 μl of GFP-expression vector pEBVCAGeGFP-Bsd kindly provided by Dr Denis Biard (CEA, iMETI, SEPIA, 750 ng/μl) mixed with Fast green were manually microinjected through the uterine wall into the cerebral lateral ventricle of embryos using a calibrated glass micropipette. Dorsal telencephalons were then electroporated across the uterus using two 3 mm paddle electrodes positioned on either side of the head and controlled by an electoporator (NEPA21, Sonidel). The electroporator delivered 4 pulses of 50ms at 30mV with a 950ms interval. The uterus was bathed with warmed phosphate buffer saline (PBS) (pH 7.4) throughout the surgical procedure. After the procedure, the uterus was placed back in the abdominal cavity and the wound was surgically sutured.

Irradiations were performed with a ^{137}Cs source (GSR-D1 irradiator, GSM GmbH) (dose rate: 0.8 Gy/min).

Sensorimotor testing of mouse pups

A series of successive sensorimotor tests, adapted from Fox's battery of tests (Fox 1965), was carried out throughout the neonatal period to assess the pre-weaning development of motor and sensory abilities in pups. Three sensorimotor tests were performed on postnatal day 3, 6 and 9, average age for successful test. We used a minimum of five litters per strain with at least six pups per litter. All pups, irrespective of their sex, were tested individually and randomly in the following order: surface righting reflex, negative geotaxis test and cliff avoidance test. Three successive trials were performed per test. Pups were separated from the dams for no more than 5 minutes to prevent maternal deprivation and hypothermia. These tests provided information concerning motor and vestibular development by measuring vestibular function, motor strength and coordination. Data from each pup of all litters were collected and averaged to yield a litter mean score used as the unit for statistical analyses.

Surface righting reflex

Each pup was placed in a supine position on a plane surface and held for 5 seconds. The time taken by the pup to return to prone position by touching all the four paws on the ground was recorded and scored within limited duration of 10 seconds per trial.[78,79] The time required to perform these tests were recorded and scored: a score of "0" was allocated to the pup that could not succeed after 10 seconds, "1" if the reflex was performed within 10 seconds, "2" if within 5 seconds and "3" if less than 2 seconds. A score of 2 was considered successful.

Negative geotaxis reflex

Each pup was placed head downward on a surface sloped by 45° and held for 5 seconds. The time taken by the pup to turn upward (180° rotation) and begin crawling up the slope was recorded and scored within limited duration of 30 seconds per trial.[78,79] This test was an innate response to gravitational cues to orient the body up slope on an inclined surface.[80] The time required to perform these tests were recorded and scored: a score of "0" was allocated to the pup that could not succeed after 30 seconds, "1" if the reflex was performed within 30 seconds, "2" if within 20 seconds and "3" if less than 10 seconds. A score of 2 was considered successful.

Cliff aversion test

Each pup was placed on an edge of a box with their forepaws and their snout over the edge. The time taken by the pup to avoid the cliff and move away from the edge more than 45° horizontal angle from the start point was recorded and scored within limited duration of 30 seconds per trial.[78,79] The time required to perform these tests were recorded and scored: a score of "0" was allocated to the pup that could not succeed after 30 seconds, "1" if the reflex was performed within 30 seconds, "2" if within 20 seconds and "3" if less than 10 seconds. A score of 2 was considered successful.

Behavioral phenotyping of adult mice

Behavioral tests were performed on 3-4-month-old male mice under a digital camera, which was connected to a computer under the control of the EthoVision video-tracking system (Noldus).

Open-Field

The open field was a squared arena (50 x 50 x 40.5 cm) with grey plexiglas floor surrounded by grey plexiglas walls, illuminated by a direct overhead lighting (55 lux).[81] Mice were individually placed in a corner of the open field and left to freely explore the apparatus for 5 min. The total distance travelled ant the time of immobility in the arena was recorded as a measure of locomotor activity. Time spent in the central part (a square of 25.5 cm side) of the open field was automatically recorded and used as a measure of anxiety.

Novel object recognition test

This[32] test was used to assess recognition memory. During the familiarization phase, two similar objects were placed in the arena on opposite corners, and mice were allowed to explore the arena for 5 min. Mice were returned to their home cages for 60 min before a second 5-minute trial. In the testing trial, mice were presented with the familiar object from the previous trial and a novel object. The objects used were T25 cell culture flask filled with clean bedding and a Lego® brick. Sessions were recorded by an overhead camera, and the EthoVision software was used to measure time spent with the familiar object and the new object. The discrimination index (DI) was calculated as [(novel object interaction time − familiar object interaction time) / (total interaction time) * 100].

Y maze spontaneous alternation test

The apparatus consisted of three plastic arms equidistant from 120°. The arm walls were 8 cm high.[82] The Y-maze spontaneous alternation is based on the natural tendency of rodents to explore a novel environment, which thus tend to alternate visits between the three arms. When placed in the Y-maze, the animal is allowed to freely explore the three arms during 5 min. The number of arms entered and percentage alternation were calculated.

Rotarod

The apparatus consists of a circular rod turning at increasing speed from 4 to 40 rpm over 5 min.[83] It was used to assess motor coordination. Mice were placed on the rotating rod with a steady acceleration, and the speed at fall was registered.

Elevated Plus Maze

The arena consisted of four arms (4.5×30 cm) made of grey plastic forming a cross. Two of the opposing arms were enclosed by walls (30×14.5 cm), and the apparatus was 50 cm above the floor. This maze was used to assess anxiety-like behavior. Mice were placed in the center of the arena and allowed to explore for 5 min. The number of entries, and the time spent in open and closed arms were calculated.

Three-chamber test for sociability

Mice were tested individually in a three-chambered arena made of clear polycarbonate, illuminated by a direct overhead lighting (10 lux). Retractable doorways built into the two dividing walls controlled access to the side chambers. Each of the two outside chambers had an empty grid enclosure. The test consisted of three consecutive trials. In the first 5 min trial (habituation), the test mouse was placed in the center chamber, and was allowed to freely explore the entire apparatus, with the empty grid enclosures. In the next 5 min trial (sociability), an unknown male (a 3-month-old NMRI male mouse), was placed in one of the two grid enclosures, while a Lego™ brick was introduced in the other grid enclosure. The object/mouse sides were alternated left and right between subjects. In the last 5 min trial, the object was replaced by another unknown male (a 3-month-old NMRI male mouse). Automatic monitoring recorded and scored the time spent in each chamber using the EthoVision video-tracking system.

Forced swim test (FST)

The mice were tested with the forced swimming test which allows to detect a depressive-like behavior.[31] The device consists of a 2-liter beaker (20 cm of diameter) filled with one liter of water (a depth of at least 10 cm) at room temperature. The mouse is placed in water for five minutes. During this period, the time spend to swim or staying immobile is measured. Floating is defined as lack of swimming with minimal movement of one leg. The total number of seconds spent floating over the course of the 5-min trial may be considered to reflect a measure of behavioral despair. Then the mouse is removed from the water, dried and returned to its cage.

Magnetic resonance imaging (MRI)

Magnetic resonance imaging was performed on a 11.7 T MRI scanner equipped with a CryoProbe (Biospec, Bruker BioSpin, Germany). *Wt* and *Xlf*-/- mice were anesthetized using isoflurane (1-2%). Body temperature was monitored and maintained at 37°C±0.5 °C. The MRI protocol consisted in 3D multi-gradient echo (T_2*-weighted) for whole-brain anatomic imaging (TE/TR=2.2/90 ms, 100 μm isotropic resolution).

These T_2*-weighted anatomical images were used to compute the individual volumes of the grey matter (GM), white matter (WM), cerebrospinal fluid (CSF), whole brain (WM + GM) and of our regions-of-interest (cerebellum, cortex, hippocampus, hypothalamus, thalamus, striatum, midbrain, olfactory bulb, corpus callosum and white matter excluding corpus callosum) using a semi-automatic segmentation pipeline. First, the GM, WM and whole brain masks were obtained with SPM (Ashburner and Friston 2005) (https://www.fil.ion.ucl.ac.uk/spm/), by the co-registration of the T_2*-weighted MRI on the GM and WM prior provided with the Turone Mouse Brain Template Atlas (TMBTA).[84] As the CSF prior was not fully satisfactory for *in vivo* studies, we exploited the high contrast between brain tissue and CSF in the T_2*-weighted MRI to better delineate the CSF mask through semi-automatic contours detection with ITK-Snap (www.itksnap.org). Additionally, the individual T_2*-weighted MRI were non-linearly co-registered with FSL[75,76] (https://fsl.fmrib.ox.ac.uk/fsl/fslwiki/) onto the TMBTA template, from which we computed the masks for our 10 regions-of-interest (ROIs). This mathematical transformation was then inverted and applied to the ROIs in the TMBTA referential to obtain the 10 corresponding ROIs in the original anatomical MRI space. The volumes were finally calculated as the number of the pixels contained in each mask, multiplied by the MRI resolution (100x100x100 μm^3). One *wt* mice was excluded because of hydrocephaly.

Antibodies

Antibodies used were: rabbit anti-Pax6 (Cell Signaling, 60433, 1:300), mouse anti-βIII (Biolegend, BLE801202, 1:500), rabbit anti-cleaved-caspase 3 (Cell signaling, 9661, 1:300), mouse anti-Ki67 (Becton Dickinson, 550609, 1:200), mouse anti-phospho H3 (Cell Signaling, 9606S, 1:300), chicken anti-GFP (Novus, NB100-1614, 1:200), mouse anti-BrdU (GE Healthcare, RPN20AB, 1:300), rabbit anti-Cux1 (Proteintech, 11733-1-AP, 1:2000), rabbit anti-Bcl11b/Ctip2, (Proteintech, 55414-1-AP, 1:2000), chicken anti-MBP (Merck, AB9348, 1:100), rabbit anti-53PB1 (Novus, NB100-304, 1:200), rabbit anti-Olig2 (Proteintech, 13999-1-AP, 1/300), mouse anti-CC1 (Abcam, ab16794, 1:300), goat anti-rabbit Alexa Fluor 488 or 594 conjugated secondary antibody (ThermoFischer, 1:400) or goat anti-chicken Alexa Fluor 488 conjugated secondary antibody (ThermoFischer; 1:400), goat anti-chicken Alexa Fluor 647-conjugated secondary antibody (Thermo-Fisher Scientific, 1:1000), and goat anti-mouse Alexa Fluor 594 (ThermoFisher, A11005, 1:400).

Histological analysis

Pregnant mice were sacrificed humanely. Embryonic heads were fixed overnight at 4°C by immersion in 4% paraformaldehyde (PFA) and embedded in paraffin with a Tissu-tek processor (VIP, Leica, Wetzlar, Germany). Five μm coronal sections were then obtained using a microtome (Leica RM2125RT) and mounted onto glass slides for histologic analyses. PN10 mouse brains were directly extracted and fixed overnight at 4°C by immersion in 4%. For analyzes adult brains, mice were perfused with saline solution and, after complete blood removal, with 4% PFA. Once extracted, the brains were fixed overnight at 4°C by immersion in 4% PFA, placed in PBS and embedded in paraffin with a Tissu-Tek processor (VIP, Leica, Wetzlar, Germany). Coronal sections (5 μm) were obtained using a microtome (Leica RM2125RT) and mounted onto glass slides for histologic analyses.

After paraffin removal and citrate treatment, the brain sections were incubated for 2 h with 7.5 % fetal bovine serum, 7.5 % goat serum in PBS. The sections were incubated with primary antibodies overnight at 4°C. After washing, the sections were incubated with appropriate secondary antibodies for 1h. After washes, nuclear staining was achieved by incubation with 4'-6-Diamidino-2-phenylindole (DAPI). Slides were mounted under Fluoromount (Southern Biotechnologies associates, Birmingham, AL, USA). For PN10 and adult brains, automated immunostainings were performed on the VENTANA BenchMark ULTRA (Roche).

Confocal pictures acquisitions were performed using a Nikon A1R confocal laser scanning microscope system attached to an inverted ECLIPSE Ti (Nikon Corp., Japan) with a 20X objective (NA 0.75). Widefield pictures were acquired using a 50i fluorescence microscope (50i, Nikon, Japan) with a 10X (NA= 0.3) or 20X (NA= 0.7) objective.

The spindle orientation of mitotic RGC was defined as the angle formed by the virtual line passing through spindle poles and the ventricular edge using an especially developed macro as previously described.[85,86]

Chromosome instability

Pregnant mice were humanely sacrificed. Embryonic cortices were then mechanically dissociated. Cells were resuspended in a hypotonic solution (37.5 mM KCl, 8.33% fetal calf serum), then incubated for 15 min at 37°C and finally fixed by a mix of acetic